

Numerical Methods for the Design and Description of In Vitro Expansion Processes of Human Mesenchymal Stem Cells



Valentin Jossen, Dieter Eibl, and Regine Eibl

Contents

1	Introduction	189
2	In Vitro Expansion Approaches: Current Situation	191
2.1	Planar Approach (2D Cultures)	191
2.2	Dynamic Approach (3D Cultures)	193
3	Computational Fluid Dynamics as a Modern Tool for Bioreactor Characterization	200
3.1	Modelling Approaches	201
3.2	Advanced Fluid Flow Characterization of Small-Scale Spinner Flasks: A Case Study	202
4	Mathematical Growth Modelling of MC-Based hMSC Expansions	216
4.1	Modelling Approaches	216
4.2	Kinetic Growth Model for the MC-Based hMSC Expansion: A Case Study	217
5	Conclusions and Outlook	221
	References	222

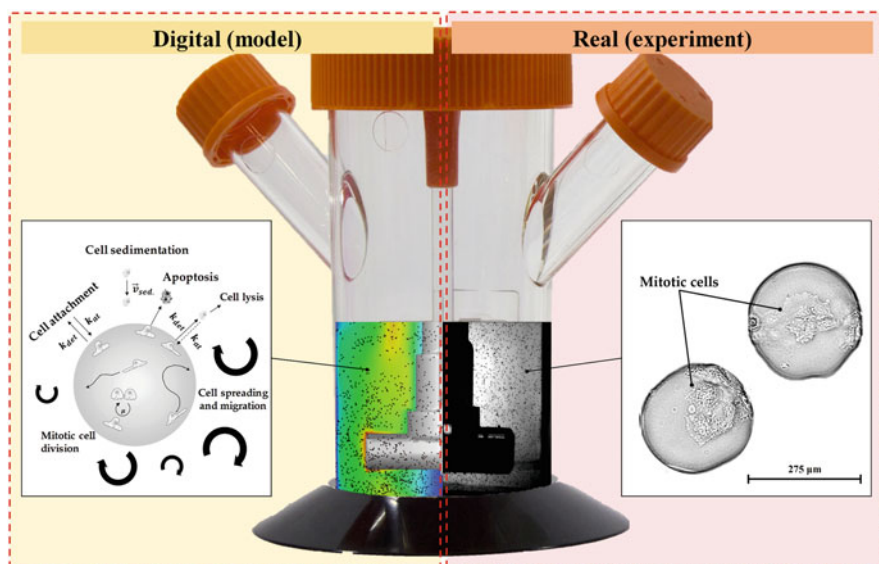
Abstract Human mesenchymal stem cells (hMSCs) are a valuable source of cells for clinical applications (e.g., treatment of acute myocardial infarction or inflammatory diseases), especially in the field of regenerative medicine. However, for autologous (patient-specific) and allogeneic (off-the-shelf) hMSC-based therapies, in vitro expansion is necessary prior to the clinical application in order to achieve the required cell numbers. Safe, reproducible, and economic in vitro expansion of hMSCs for autologous and allogeneic therapies can be problematic because the cell material is restricted and the cells are sensitive to environmental changes. It is beneficial to collect detailed information on the hydrodynamic conditions and cell

V. Jossen (✉), D. Eibl, and R. Eibl
Zurich University of Applied Sciences – Institute of Chemistry and Biotechnology, Wädenswil,
Switzerland
e-mail: valentin.jossen@zhaw.ch

growth behavior in a bioreactor system, in order to develop a so called “Digital Twin” of the cultivation system and expansion process. Numerical methods, such as Computational Fluid Dynamics (CFD) which has become widely used in the biotech industry for studying local characteristics within bioreactors or kinetic growth modelling, provide possible solutions for such tasks.

In this review, we will present the current state-of-the-art for the *in vitro* expansion of hMSCs. Different numerical tools, including numerical fluid flow simulations and cell growth modelling approaches for hMSCs, will be presented. In addition, a case study demonstrating the applicability of CFD and kinetic growth modelling for the development of an microcarrier-based hMSC process will be shown.

Graphical Abstract



Keywords Computational Fluid Dynamics, Euler-Euler model, Euler-Lagrange model, Human mesenchymal stem cells, Kinetic growth modelling, Microcarrier technology, Single-use bioreactor

Abbreviations

CC	Collagen-coated
CFD	Computational Fluid Dynamics
DMEM	Dulbecco's Modified Eagle Medium
DSP	Downstream processing

ECM	Extracellular matrix
bFGF	Basic fibroblast growth factor
FBS	Fetal bovine serum
GMP	Good manufacturing practice
hASC	Human adipose tissue-derived stromal/stem cells
hBM-MSC	Human bone marrow-derived mesenchymal stem cells
hMSCs	Human mesenchymal stem cells
hPL	Human platelet lysate
HGF	Hepatocyte growth factor
HSB	Hemispherical-bottom bioreactor
LDA	Laser Doppler Anemometry
LES	Large Eddy Simulations
α MEM	Modified Eagle Medium
MC	Microcarrier
MCB	Master Cell Bank
MRF	Moving reference frame
OTR	Oxygen transfer rate
PIV	Particle Image Velocimetry
PS	Polystyrene-based
RB	Round-bottom bioreactor
RMSD	Root mean square deviation
SIMPLE	Semi-implicit method for pressure-linked equations
SM	Sliding mesh
SU	Single use
UCM	Umbilical cord-derived mesenchymal stem cells
USP	Upstream processing
VEGF	Vascular endothelial growth factor
VOF	Volume of fluid
WCB	Working Cell Bank

Latin Symbols

Amn (mmol/L)	Ammonium concentration
D_{O_2} (m ² /s)	Oxygen diffusivity
D_R (m)	Vessel diameter
EF	Expansion factor
F (N)	Force
Glc (mmol/L)	Glucose concentration
h/H_L	Geometrical ratio between a certain height and the liquid height
h_R/D_R	Geometrical ratio between impeller installation height and the vessel diameter (= off-bottom clearance)
H_L (m)	Liquid height
H_L/D	Geometrical ratio between liquid height and vessel diameter

k_{at} (d^{-1})	Cell attachment constant
k_{det} (d^{-1})	Cell detachment constant
K_{Amn} (mmol/L)	Inhibition constant of ammonium
K_{Glc} (mmol/L)	Monod constant of glucose
K_{Lac} (mmol/L)	Inhibition constant of lactate
Lac (mmol/L)	Lactate concentration
N (rpm)	Impeller speed
N_{sLu} (rpm)	Lower limit of N_{sI} suspension criterion
N_{sI} (rpm)	1s or just suspended criterion (=N _{js})
PDL	Population doubling level
P/V (W/m^3)	Specific (volumetric) power input
p_{Amn} (mmol/cell/d)	Specific ammonium production rate (growth-independent)
p_{Lac} (mmol/cell/d)	Specific lactate production rate (growth-independent)
q_{Amn} (mmol/cell/d)	Specific ammonium production rate (growth-dependent)
q_{Glc} (mmol/cell/d)	Specific glucose consumption rate
q_{Lac} (mmol/cell/d)	Specific lactate production rate (growth-dependent)
Re	Reynolds number
r/R	Dimensionless radial coordinates
t_c (s)	Contact time
t_{cir} (s)	Particle circulation times
t_d (d)	Doubling time of cell population
t_l (d)	Lag or cell adaption time
t_{res} (s)	Particle residence time
u_{tip} (m/s)	Impeller tip speed
\vec{u} (m/s)	Velocity vector in x-direction
V_{min} (mL)	Minimal working volume
V_{max} (mL)	Maximum working volume
\vec{v} (m/s)	Velocity vector in y-direction
\vec{w} (m/s)	Velocity vector in z-direction
X_A (cells/cm ²)	Cell concentration on surface
X_{max} (cells/cm ²)	Maximum cell concentration on surface
X_{Sus} (cells/mL)	Cell concentration in suspension
X_V (cells/cm ²)	Cell concentration of viable cells ($X_{Sus} + X_A$)
$Y_{Lac/Glc}$ (mmol/mmol)	Lactate yield per glucose equivalent
Y_{X/O_2} (1/mmol)	Yield coefficient/cells per mmol oxygen

Greek Symbols

α	Cell adaption phase coefficient
α_{MC}	MC volume fraction
δ_{Glc}	Step response in glucose balance to avoid negative glucose values ($\delta_{Glc} = 0$ or 1)
η_L (Pa s)	Dynamic viscosity of the liquid

π	Mathematical constant (≈ 3.1415)
ρ_L (kg/m ³)	Density of the liquid
τ_{nn} (Pa)	Local normal stress
τ_{nt} (Pa)	Local shear stress
μ (1/d)	Specific growth rate
μ_{max} (1/d)	Maximum specific growth rate

1 Introduction

The successful development and application of cell-based therapies have the potential to treat a number of currently incurable diseases and to improve patient care. It is therefore not surprising that cell-based therapies have become increasingly important in the field of regenerative medicine, as the expected revenue for 2020 of up to US\$ 6.09 billion indicates [1]. Special attention in the field of regenerative medicine is currently being paid to human mesenchymal stem cells (hMSCs). This is unsurprising due to their existence in postnatal tissues (e.g., adipose tissue, bone marrow, the umbilical cord), their high proliferation potential, and their immunosuppressive, immunoregulating, migrating, and trophic properties and low ethical concerns. At the beginning of 2020, 41 clinical trials involving hMSCs were registered (www.clinicaltrials.gov). In addition to the large number of currently ongoing clinical studies, 17 hMSC-based products have received marketing authorization to date (see Table 1), demonstrating the need for reproducible and robust cell processing methods. Product manufacturing takes place mainly with mesenchymal stem cells derived from human bone marrow (hBM-MS; 11 products), followed by adipose tissue-derived stem cells (hASCs; 5 products).

In general, hMSC-based therapies can be broadly divided into two categories: patient-specific therapies (autologous) and off-the-shelf therapies (allogeneic). From an economic point of view, the allogeneic therapy approach seems to be the most attractive option at present [2, 3]. However, independent of the therapy approach, an in vitro expansion of hMSCs is required to deliver an effective therapeutic dose (1–5 million hMSCs/kg body weight [4–6]). The intention of the in vitro expansion step is to manufacture a sufficient number of hMSCs under good manufacturing practice (GMP) conditions and in a cost-effective manner. It is clear that in vitro manufacturing of hMSCs is often difficult because the cells, which are the product, are directly isolated from body tissue and are genetically unstable in vitro (e.g., cellular senescence) [7]. In addition, significant differences in the cell yield, the proliferation rate, and the differentiation potential have been found between different donors, as well as for different ages of donor and health conditions [8–10]. Apart from the biological variability of the cell material, hMSCs are also sensitive to environmental changes and chemical and physical stresses [11, 12]. As a result, all these aspects place high demands on the in vitro cell expansion process. MSC manufacturing is characterized

Table 1 Available hMSC-based products (as of May 2020)

Medicinal product	Company	Therapy/cell type	Indication	Market
Allostem	AlloSource	Allogeneic ASC	Bone regeneration	USA
Alofisel	TiGenix-Takeda	Allogeneic ASC	Anal fistula in Crohn's disease	EU
AstroStem	Biostar	Autologous ASC	Alzheimer's disease	Japan
aJointStem	Biostar	Autologous ASC	Degenerative arthritis	Japan
Cartistem	Medipost	Allogeneic UCM	Degenerative arthritis	Korea
Cupistem	Anterogen	Allogeneic ASC	Anal fistula in Crohn's disease	Korea
Grafix	Osiris Therapeutics	Allogeneic BM-MSC	Soft tissue defects	USA
HearticellGram-AMI	FCB PharmiCell	Autologous BM-MSC	Acute myocardial infarction	Korea
Neuronata-R	Corestem	Allogeneic BM-MSC	Amyotrophic lateral sclerosis	Korea
OsteoCel	NuVasive	Allogeneic BM-MSC	Spinal bone regeneration	USA
OvationOS	Osiris Therapeutics	Allogeneic BM-MSC	Bone regeneration	USA
Prochymal	Osiris Therapeutics	Allogeneic BM-MSC	Acute graft vs. host disease	Canada
Stemirac	NIPRO Corp	Autologous BM-MSC	Spinal cord injury	Japan
Stempeucel	Stempeutics	Allogeneic BM-MSC	Critical limb ischemia	India
TemCell	JCR Pharm.	Allogeneic BM-MSC	Acute graft vs. host disease	Japan
Trinity Elite	Orthofix	Allogeneic BM-MSC	Bone regeneration	USA
Trinity Evolution	Orthofix	Allogeneic BM-MSC	Bone regeneration	USA

by different manufacturing steps covering upstream processing (USP), downstream processing (DSP), formulation, and fill and finish operations. Typical USP operations are the manufacturing of the Master Cell Bank (MCB) and Working Cell Bank (WCB), seed cell production, and cell expansion at L-scale. DSP operations include cell harvest, cell separation, washing as well as concentration procedures, and medium exchange. Different economic studies have demonstrated that the USP, and in particular the hMSC expansion, represents the main cost driver when examining the whole manufacturing process [3, 13, 14]. To reduce the number of experiments and to increase the process knowledge during either the design and development or the optimization phase, virtual representations of the hMSC production process, so called “Digital Twins,” are helpful. These virtual models allow an approximation of real process conditions, a fact that is particularly important for

the production of cell therapeutics, as, among other things, cell material (in an autologous approach) may vary between batches. Process conditions must, therefore, be adapted to the biological starting material, increasing the complexity of the production process. Here application of a “Digital Twin,” which combines biochemical engineering data of the cultivation system with a mathematical model of the cell growth, is beneficial, as it tests different process conditions *in silico* and subsequently proposes optimal parameter combinations for the hMSC production process.

2 In Vitro Expansion Approaches: Current Situation

For the clinical application of hMSCs, the *in vitro* expansion of the cells represents an important step. Although recent studies have shown the difference in cell yield depending on the hMSC source (e.g., bone marrow vs. adipose tissue), the required therapeutic dose (1–5 million hMSCs/kg body weight) makes *in vitro* expansion mandatory independent on the hMSC-type. Therefore, different systems and cultivation strategies have been developed over the years for the expansion of hMSCs, which will be presented and discussed in the following sections.

2.1 Planar Approach (2D Cultures)

hMSCs are typically isolated by their capacity to adhere to plastic surfaces. Therefore, the simplest way to expand hMSCs is the usage of plastic vessels, such as T-flask or stacked plate systems, which allow for the expansion of the cells at laboratory and pilot plant production scale for early-phase clinical trials [15]. Planar expansion approaches in normal cell culture flasks (e.g., T-flasks) represent a cost-efficient and easy-to-operate solution. Maximum cell densities for hMSCs from the human bone marrow, the adipose tissue, and the umbilical cord have been reported in the literature in the range of 0.05 to 1.0×10^5 cells/cm² (PDL 2.8–7.4) for T-flask cultures performed with serum-containing and serum-free cell culture medium (see Table 2). Maximum cell densities for CellSTACK cultures were even reported in the range of 2.5 to 4.2×10^5 cells/cm² ($=1.59$ – 2.67×10^9 cells) using hMSCs from the bone marrow.

However, scale-up of such an hMSC expansion process would require a large number of cell culture flasks, which is by any means neither economic nor ecologic. Moreover, handling of multiple flasks in parallel is very labor and cost intensive (increased facility footprint) and may result in high flask-to-flask variabilities. In addition, the risk of contamination (e.g., bacteria, mycoplasmas) is increased due to the large number of open manipulations. Alternatives to the normal cell culture flasks are stacked-plate or multi-tray culture systems, such as cell factories, which significantly increase the efficiency of the cultivation step by using several layers per cultivation system (up to 40-layer systems available). Thus, the absolute cell number

Table 2 Overview of hMSC expansions in different static, planar cultivation systems

MSC type	2D cultivation system	Culture medium	Cell density	PDL	Ref.
hBM-MSC	T-flask (Greiner)	α MEM + 15 % FBS	$0.05-0.6 \times 10^5$ cells/cm ²	5.6 ± 1.8	[10]
	T-flask (CellBIND)	Corning stemgro hMSC	1.0×10^5 cells/cm ²	4-5	[16]
	CellSTACK-5	DMEM/ α MEM + hPL	$0.4-0.9 \times 10^5$ cells/cm ²	n/a	[6]
	CellSTACK-10	BD Mosaic SFM	2.5×10^5 cells/cm ²	n/a	[17]
	CellSTACK-10	DMEM + 10 % FBS	4.2×10^5 cells/cm ²	n/a	[17]
	Nunc Cell Factory-4	α MEM + 10 % FBS	1.8×10^5 cells/cm ²	4.9	[18]
hASC	T-flask (Corning)	UrSuppe SFM	0.7×10^5 cells/cm ²	2.8-3.2	[19]
UCM	T-flask (Sarstedt)	DMEM + 10 % FCS	0.5×10^5 cells/cm ²	4.9	[20]
	CellSTACK-5	DMEM/ α MEM + hPL	$1.6-1.8 \times 10^5$ cells/cm ²	n/a	[6]

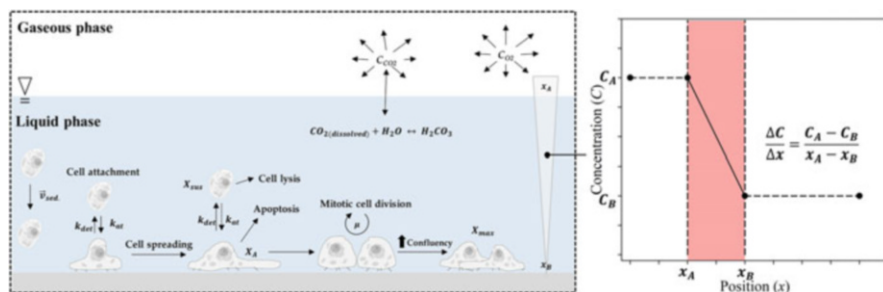


Fig. 1 Schematic representation of biochemical and physical parameters, which have an influence on planar hMSC cultures

per cultivation is significantly increased. Maximum cell densities have been reported in the literature in the range of 0.4 to 4.2×10^5 cells/cm² for hMSCs expanded in 5- and 10-layer multi-tray systems with serum-containing and serum-free cell culture medium (see Table 2). Due to the static nature of the multi-tray systems, there is always the risk of gradients in pH and pO₂ levels in the liquid phase, possibly introducing heterogeneities that affect cell growth and quality (see Fig. 1). Moreover, the lack of sensors in the systems does not allow the maintenance of optimal set points for some physiochemical parameters (e.g., pH and pO₂), resulting in fluctuating conditions for the cells. The multi-tray systems are also not fully closed, meaning that open manipulations are routinely performed, which require clean room facilities and a class-A laminar flow hood for each manipulation. Interestingly, to date the main reviews on hMSC clinical trials specify that clinical grade cells have mainly been expanded in static 2D systems [6, 15, 21, 22]. However,

in terms of GMP requirements, alternative procedures and cultivation systems, like the spheroid- or microcarrier-based expansion in stirred single-use bioreactors, are said to be the platforms for future cell therapeutic productions (see Sect. 2.2).

2.2 *Dynamic Approach (3D Cultures)*

As mentioned in Sect. 2.1, hMSCs are typically expanded under adherent conditions as a monolayer in 2D culture systems. However, isolation and growth of hMSCs on rigid tissue culture plastic have been described as promoting spreading of cells rich in actin-myosin stress fibers [23, 24]. Indeed, the static 2D culture systems represent an artificial environment which significantly differs from those of the MSC in vivo niche. Therefore, different efforts have been made over the years to establish dynamic 3D culture systems working with spheroids (see Sect. 2.2.1) or microcarriers (see Sect. 2.2.2). In dynamic bioreactor systems (stirred, wave-mixed, orbitally shaken, hollow fiber and fixed bed types), the culture medium is continuously agitated to provide a uniform environment, preventing the formation of physiochemical gradients and improving mass and heat transfer. Special attention is currently being paid to SU versions, which significantly improve patient safety [25]. Even though different studies have recently shown the applicability of SU systems for MC-based hMSC production processes, challenges still exist.

For this reason, it makes sense to characterize the different bioreactor systems using appropriate process engineering and cell cultivation technique methods prior to usage or during process development, simultaneously assisting in the development of a “Digital Twin.” Several studies have been published that provide engineering parameters relating to mixing time, oxygen mass transfer, and power input for various SU bioreactor types. However, when considering the heterogeneous distribution of MCs, spheroids and hydrodynamics, and a detailed analysis of the fluid flow pattern, the MC distribution and the cell growth become worthwhile. Numerical methods, such as Computational Fluid Dynamics (CFD) and kinetic growth models, are complementary methods to the experimental investigations and increase the process knowledge of hMSC production methods. Thus, numerical models can be used to support process development and scale-up.

2.2.1 **Growth in Spheroids**

hMSCs are often expanded in stirred SU bioreactors as self-assembling cell aggregates or spheroids that mimic the in situ conditions. Thus, compared to 2D monolayer cultures, 3D structures consisting of multiple cell-to-cell contact points are obtained. However, due to their heterogeneous nature, spheroids have been more successfully employed to study complex 3D cell structures and cell differentiation [26] than for hMSC mass expansion in stirred SU bioreactors, as indicated by the limited number of publications in this area (see Table 3).

Table 3 Bioreactors operated with spheroids

MSC type	Bioreactor system	N	Medium	Seeding	D_{max}	Ref.
hBM- MSC	100 mL Techne spinner	30 rpm	α MEM+15% FBS	0.2×10^5 cells/mL	135 μ m	[27]
	125 mL Shake flask	80 rpm	SFM medium	1×10^5 cells/mL	n/a	[28]
	125 mL Paddle bioreactor	80 rpm	PPRF-msc6	0.5×10^5 cells/mL	218 μ m	[29]
hASC	100 mL BellCo spinner	70 rpm	α MEM+10% FBS	6×10^5 cells/mL	350 μ m	[30]

The main motivation for growing hMSCs as spheroids is to avoid the use of exogenous support materials, like scaffolds or MCs. Due to the absence of the exogenous support material, the cells are allowed to arrange themselves similar to living tissues [22, 31]. Cells self-assemble and interact under natural forces, permitting them to generate their own extracellular matrix (ECM), which serves as support for the cells to survive in suspension and to mimic the cell-to-cell and cell-to-matrix signaling networks [32, 33]. Investigations by Edmonson et al. [34] have shown that the cell morphology of hMSCs derived from spheroid cultures is comparable to those in bodily tissues. In addition, Caron et al. [35] have demonstrated that a stable hMSCs phenotype is retained in spheroid-based cultures, at least when only the minimum definition of an hMSC is considered [36, 37]. A study by Cheng et al. [38] highlighted that spheroid-derived hASCs exhibited lower cell senescence and a high secretion of angiogenic growth factors (e.g., HGF, VEGF), which was found to be beneficial for wound healing applications. Interestingly, several studies with hBM-MSCs have found that the 3D structure of the spheroids leads to higher yields of secreted immunomodulatory paracrine and anti-inflammatory factors (i.e., TSG-6, stanniocalcin-1, prostaglandin E2) [39, 40], although this was highly dependent on the cell culture medium formulation [41, 42]. The cell culture medium and its formulation play a critical role in spheroid-based hMSC expansions. For example, Zimmermann and McDevitt [41] found that hBM-MSCs expanded in serum-free cell culture medium displayed a reduced expression of prostaglandin E2, indoleamine 2,3-dioxygenase, transforming growth factor- β 1, and interleukin-6 when compared with spheroids cultured in serum-containing cell culture medium. Since the cells are forced to aggregate to form spheroids, the medium must also contain adhesive molecules (e.g., laminins, integrins, E-cadherin, vitronectin) to facilitate cell-to-cell attachment [43]. However, for GMP-compliant hMSC productions, these recombinant human proteins represent a strong cost driver, which makes large-scale manufacturing expensive [44]. In addition to biochemical parameters, physical or process engineering parameters have a strong effect on the spheroid culture (see Fig. 2).

For example, oxygen tension has been shown to play a fundamental role in the spheroid formation. Spheroids generated in hypoxic conditions (2% O_2) produced higher amounts of ECM components (i.e., fibronectin, laminin, elastin) and higher

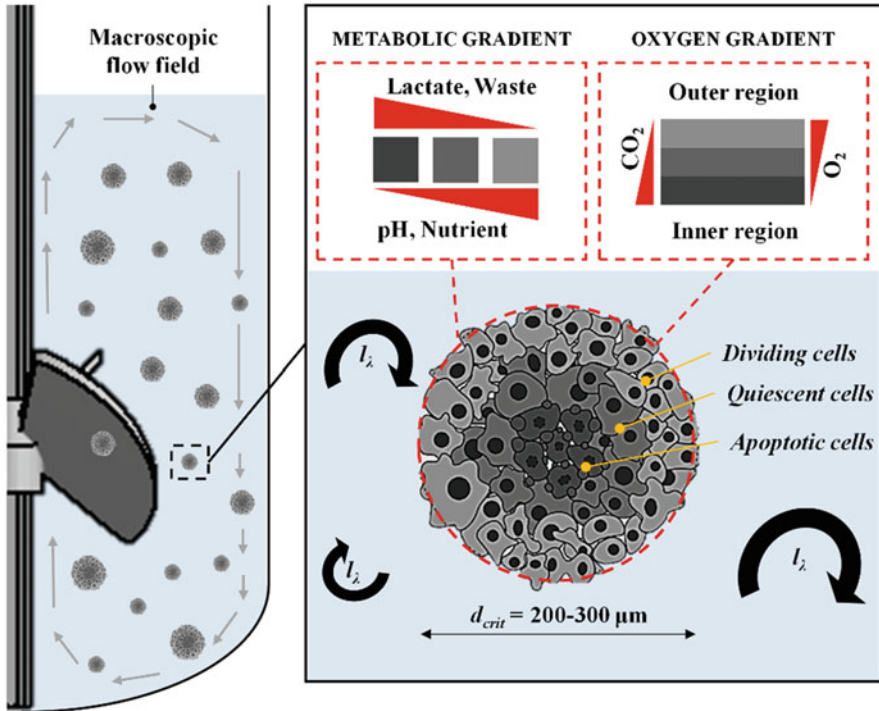


Fig. 2 Schematic representation of biochemical and physical parameters that have an influence on hMSC spheroid cultures

amounts of growth factors (i.e., VEGF, bFGF) [45]. Therefore, spheroids are effective for the tuning of specific cell features but limited in terms of cell proliferation. Bartosh et al. [39] have shown that proliferation-related genes are downregulated in hMSCs upon aggregation. Thus, maximum cell densities in spheroid-based cultures are limited to a certain spheroid size and to the number of spheroids formed in the bioreactor, which limits their applicability for the hMSC mass expansion. Moreover, large spheroids are exposed to diffusional limitations (e.g., oxygen and nutrients), which is a major drawback in high cell density cultures. Different studies have highlighted that spheroids exceeding 200–300 μm tend to induce apoptosis or even undesired spontaneous differentiation due to nutrient or oxygen limitations in the core of the spheroids [46–48]. Indeed, the size of the spheroids can be controlled to a certain level by the fluid flow regime in a stirred bioreactor, but this strategy provides another level of complexity, since spheroid breakage procedures need to be introduced throughout the process. Various studies have shown that the hydrodynamic stresses, the fluid velocities, and the Kolmogorov length scale are very heterogeneously distributed in stirred bioreactors [12, 49, 50], which may limit their effect on the spheroid size. Thus, spheroids are exposed to fluctuating hydrodynamic stresses. Novel bioreactor designs are required that

provide homogenous shear stress levels for the formation and regulation of the spheroid sizes. Such bioreactor development or design studies can be supported by numerical models that allow for optimization of the fluid flow regarding these issues (i.e., homogenous hydrodynamic stress distribution).

2.2.2 Growth on Microcarriers

In order to overcome the limitations of the 2D culture systems, in 1967 van Wezel [51] developed the concept of MC-based cultivation systems. In these systems, the cells are expanded on the surface of small solid particles suspended in the cell culture medium by slow agitation. The MC-based expansion represents a unit operation in which both monolayer and suspension cultures are brought together. The MC surface is available for cell growth, while the mobility of MCs in the medium generates a homogeneity that is similar to the suspension environment used in traditional mammalian submerged cultures [52]. Thus, MC-based expansion systems offer the following advantages:

1. A high surface to volume ratio, which can be further increased by increasing the MC concentration
2. A homogenous environment that allows various process parameters (e.g., pH, pO_2 , substrates and metabolites) to be both monitored and controlled
3. A possible scale-up of the MC-based expansion process within a suitable bioreactor series
4. Functionalization of the MC surface to improve cell attachment and in terms of hMSCs to retain a high “stemness”

Different MCs, which are usually spherical, have been tested or even developed over the years for the expansion of hMSCs (see Table 4). The MC types differ greatly in size (90–380 μm), core material (e.g., polystyrene, cellulose, dextran, gelatin), and surface coating (e.g., collagen, fibronectin, laminin, vitronectin). An overview of commercially available MCs, including their material properties, can be found in different reviews [15, 52, 53]. The core material and surface coating affect not only the MC settlement and cell growth but also the impeller speed which is required to hold the MCs in suspension and to guarantee sufficient mass transfer. Rafiq et al. [54] and Leber et al. [55] screened different MC types in small-scale bioreactors for hMSCs under predefined impeller speeds ($N_{js} = N_{st}$). Both found significant differences in cell attachment, cell growth, glucose consumption, and metabolite production depending on the MC type. They found that hBM-MSC grow best on collagen-coated MCs from Solohill and Synthemax II and ProNectin F MCs from Corning, something which comes as no surprise since these MCs are coated with collagen and fibronectin, respectively. Both coatings are components of the extracellular matrix, including the arginyl-glycyl-aspartic acid sequence which is well-known to promote cell attachment and cell growth of fastidious cells [56]. Different studies have shown that the planar structure, including the material stiffness, nanotopography, and local curvature, can impact cell proliferation, maintenance of

Table 4 Bioreactors operated with microcarriers for the expansion of hMSCs from bone marrow and adipose tissue

MSC source	Bioreactor system	WV	Microcarrier/coating	Culture medium	Agitation	Cell density	Ref.
hBM-MSC	100 mL BellCo spinner	100 mL	Cytodex 1 and 3	DMEM+10% FBS	30 rpm	$0.65-0.68 \times 10^6$ cells/mL	[69]
	100 mL BellCo spinner	100 mL	Polystyrene-based MC	DMEM+10% FBS	30 rpm	0.08×10^6 cells/mL (2.7-fold)	[70]
	100 mL BellCo spinner	100 mL	Polystyrene-based MC	PRIME-XV SFM	30 rpm	0.31×10^6 cells/mL (10-fold)	[67]
	100 mL BellCo spinner	80 mL	Synthemax II	StemPro MSC	40 rpm	0.36×10^6 cells/mL (8-fold)	[68]
	amb [®] 15	15 mL	Plastic	DMEM+10% FBS	400 rpm	$0.10-0.50 \times 10^6$ cells/mL	[71]
	BioBLU [®] 0.3c	250 mL	Cytodex 1 and 3	MSCGM-CD	60 rpm	0.40 and 0.28×10^6 cells/mL	[72]
	BioBLU [®] 0.3c	100 mL	Plastic+PRIME-XV FN	DMEM+10% FBS	115 rpm	0.20×10^6 cells/mL	[73]
	BioBLU [®] 0.3c	100 mL	Plastic+PRIME-XV FN	DMEM+PRIME XV	115 rpm	0.70×10^6 cells/mL	[73]
	Mobius [®] CellReady 3L	2.4 L	Collagen-coated MC	α MEM+10% hPL	25-35 rpm	0.40×10^6 cells/mL	[63]
	UniVessel [®] SU 2L	2 L	CultiSpher G	Lonza medium+5% FBS	70 rpm	0.53×10^6 cells/mL	[74]
	BIOSTAT [®] STR 50L	50 L	CultiSpher G		63 rpm	0.72×10^6 cells/mL	[75]
	Mobius [®] CellReady 50L	50 L	Collagen-coated MC	α MEM+10% hPL	64-100 rpm	0.19×10^6 cells/mL	[63]
hTERT-MSC	100 mL Integra spinner	70 mL	Glass-coated MC	DMEM+10% FBS	30-75 rpm	0.38×10^6 cells/mL	[55]
	1 L bioreactor Applikon	1 L	Glass-coated MC	DMEM+10% FBS	100 rpm	0.14×10^6 cells/mL	[55]

(continued)

Table 4 (continued)

MSC source	Bioreactor system	WV	Microcarrier/coating	Culture medium	Agitation	Cell density	Ref.
hASC	125 mL Corning spinner	100 mL	ProNectin-F	Lonza medium+5% FBS	49 rpm	$0.58-1.25 \times 10^6$ cells/mL	[11, 62]
	100 mL BellCo spinner	80 mL	Synthemax II	StemPro MSC	40 rpm	0.19×10^6 cells/mL	[68]
	BioBLU [®] 5c	3.75 L	Polystyrene-based MC	MSC medium ATCC	25-35 rpm	0.04×10^6 cells/mL	[76]
	BioBLU [®] 5c	3.75 L	Collagen-coated MC		25-35 rpm	0.24×10^6 cells/mL	[76]
	UniVessel [®] SU 2L	2 L	ProNectin-F	Lonza medium+5% FBS	100-140 rpm	0.27×10^6 cells/mL	[62]
hTERT-ASC	BIOSTAT [®] STR 50L	35 L	ProNectin-F		50-66 rpm	0.31×10^6 cells/mL	[62]
	125 mL Corning spinner	100 mL	ProNectin-F		49 rpm	0.63×10^6 cells/mL	[12]
	500 mL Corning spinner	300 mL	ProNectin-F		52 rpm	0.88×10^6 cells/mL	[12]

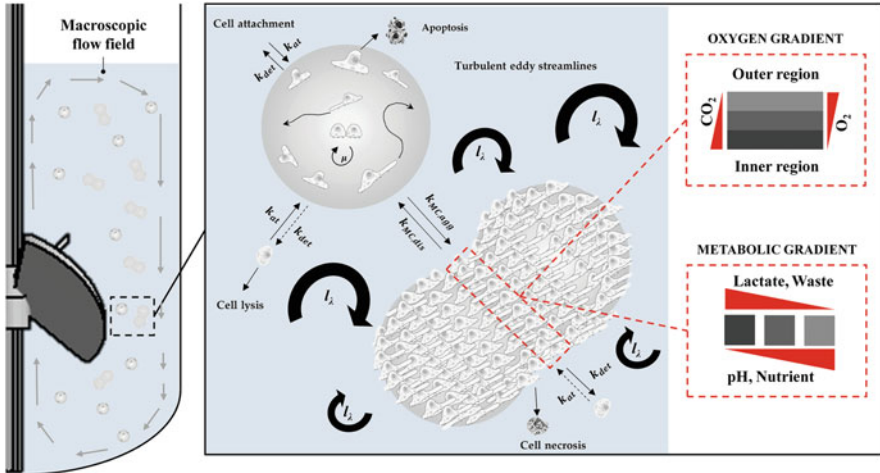


Fig. 3 Schematic representation of biochemical and physical parameters that have an influence on MC-based hMSC cultures

phenotype, and differentiation [57, 58]. Thus, many efforts are being made to develop GMP-grade biodegradable MCs. In general, cell attachment follows a Poisson distribution, where cell-to-MC ratios of one, two, or three result in theoretical probabilities of unoccupied MCs of 0.365, 0.135, and 0.05, respectively [59, 60]. Thus, theoretical cell densities for inoculation are in the range of between 3 and 5 cells per MC. After the cell attachment phase (4–20 h) under static or intermitted stirred conditions, every MC should have the same number of cells attached to its surface. However, in practice, this is not the case. As investigations by Ferrari et al. [61] have shown, suboptimal cell seeding results in the early formation of MC-cell aggregates that impair cell growth and characteristics (see Fig. 3). In addition, large MC-cell aggregates increase the risk of apoptotic cells due to the limited diffusivity of oxygen and nutrients into these aggregates. In fact, the impeller speed can be used to a certain extent to control such MC-cell aggregates, but the hydrodynamic stresses required for this task may also affect the cell growth and quality, especially of the outer cells. To minimize this risk, reliable models of the culture systems (“Digital Twins”) are necessary.

In addition to the selection of a suitable MC, the cell culture medium and its formulation also play a key role in the success of a MC-based cultivation. Many of the conventional culture media used for the expansion of hMSCs are defined basal media such as DMEM or α -MEM, which have to be supplemented with additives such as (I) proteins that mediate adhesion to the MC surface, (II) lipids for cellular anabolic purpose, and (III) growth factors and hormones to stimulate cellular proliferation and phenotype maintenance (see Table 4). Even though the disadvantages of serum are well-known, a lot of the hMSC cell culture media additionally contain 5–10% FBS. The highest cell densities generated in serum-containing

medium (10% FBS) have been reported in the range of $0.14\text{--}0.65 \times 10^6$ cells/mL for cultivations in stirred bioreactors up to benchtop scale. Schirmaier et al. [62] and Lawson et al. [63] reported maximum cell densities of up to 0.3×10^6 cells/mL for cultivations in stirred bioreactors at pilot scale with a cell culture medium supplemented with 10% hPL or 5% FBS. Jossen et al. [11] even reported maximum peak cell densities of up to 1.25×10^6 cells/mL for hMSCs from the adipose tissue in spinner flask cultures with 5% FBS. A proven alternative to FBS is human platelet lysate (5–15%). However, there is still a controversial discussion about whether the cells retain their immunomodulatory properties and their full differentiation capabilities [64–66]. Moreover, there is still a risk of human pathogens and their components being poorly characterized. Therefore, there is a high level of interest in serum- and xeno-free, chemically defined cell culture media. Various formulations are now available on the market (e.g., Mesencult-XF, MSCGM-CD, StemMACS MSC XF, etc.). The careful selection and supplementation of the XF basal medium with suitable growth factors and hormones are important, especially when working with MCs in stirred bioreactors. Special attention has to be paid to cell attachment efficiency and shear stress sensitivity. It is an established fact that the maximum cell densities ($0.04\text{--}0.40 \times 10^6$ cells/mL) and expansion factors that have been achieved in stirred bioreactors with xeno- and serum-free cell culture media are still lower than those achieved in serum-containing medium (see Table 4). Heathman et al. [67] reported a maximum cell density of 0.31×10^6 cells/mL and an expansion factor of 10 within 6 days of using PRIME-XV SF medium in a 100 mL BellCo spinner flask. Carmelo et al. [68] even achieved a maximum cell density of up to 0.36×10^6 cells/mL but a slightly lower maximum expansion factor of 8 with the StemPro MSC medium. Maximum cell densities of between 0.04 and 0.40×10^6 cells/mL were reported for the ATCC and MSCGM-CD medium in the BioBLU 0.3c and BioBLU 5c bioreactor systems.

3 Computational Fluid Dynamics as a Modern Tool for Bioreactor Characterization

Numerical methods, such as CFD, are widely used in the biotech industry to investigate local properties (e.g., flow velocities, shear stresses) in bioreactors and offer an alternative to experimental measurements (e.g., Particle Image Velocimetry (PIV), Laser Doppler Anemometry (LDA)), which are often time-consuming and expensive. Thus, it is unsurprising that CFD is also a valuable tool for the characterization of bioreactor systems used for the production of cell therapeutics. In the following section, a short overview of the basic principle of CFD and various investigations described in the literature are presented. In addition, a case study will be discussed that demonstrates the use of CFD for the characterization of two spinner flask types used for the MC-based hMSC expansion.

3.1 Modelling Approaches

The prediction of the fluid flow is based on solving mass, momentum, and energy conservation equations. This concept includes balances of accumulation, net inflow from convection and diffusion, and volumetric production within an infinitesimally small volume element. For most of the bioprocesses performed in the biotech industry, isothermal conditions (i.e., $T \approx \text{const.}$) can be assumed. As a result, the energy balance can be neglected. The mass and momentum equations for incompressible Newtonian media, which includes cell culture media, can be written as shown in Eq. (1) (*Continuity equation*) and Eq. (2) (*Momentum equation*).

$$\frac{\partial \rho}{\partial t} + \nabla \cdot (\rho \vec{u}) = 0 \quad (1)$$

$$\frac{\partial (\rho \vec{u})}{\partial t} + \nabla \cdot (\rho \vec{u} \vec{u}) + \nabla p - \nabla \tau - \rho \vec{g} + \vec{F} = 0 \quad (2)$$

Based on the balancing concept and the spatial discretization of the fluid domain, local and time-dependent data (e.g., velocity gradients, hydrodynamic stress) can be calculated and used for the bioreactor design, the bioreactor characterization, and the process development. Thus, it is unsurprising that different modelling approaches are described in the literature for the CFD-based characterization of bioreactors used for the expansion of hMSCs (see Table 5). For example, Nienow et al. [71, 77], Kaiser et al. [50], Berry et al. [77], and Schirmaier et al. [62] performed single-phase simulations in the ambr 15, the disposable Corning spinner flask, the UniVessel SU 2L, and the BIOSTAT STR 50L based on a *Reynolds-averaged Navier-Stokes (RANS)* approach in order to derive the fluid flow pattern and the hydrodynamic stresses acting under different process conditions. The *RANS* approach simplifies the formulation of the instantaneous velocities u by the sum of time-averaged velocities \bar{u} and their fluctuations u' , which reduces the computational efforts due to a lower grid resolution. In contrast, Collignon et al. [79] used a *Large Eddy Simulation (LES)* approach, which only resolves macroscopic eddies, for the fluid flow characterization of a 250 mL mini-bioreactor, and their results were found to be in accordance with experimental data. Detailed information about the different numerical models can be found in high-grade textbooks [78–80]. The single-phase simulations do not provide information about the MC distribution and their dynamics in the system. As a result, Delafosse et al. [81], Kaiser et al. [50], and Jossen et al. [11, 12] used a *Euler-Euler* approach in which the MCs were considered as secondary phase. However, this approach does not include discrete formulation of the particle phase and, therefore, only provides information for the entire phase. For this reason, Liovic et al. [82], Jossen et al. [12], and Delafosse et al. [83] described the use of a *Euler-Lagrange* approach which provides a discrete particle formulation and the tracking of individual particles in the bioreactor. Thus, they calculated the circulation and residence times as well as the hydrodynamic stresses acting on individual particles and used this information for process development and characterization.

Table 5 Overview of studies dealing with CFD in order to characterize bioreactor systems for the expansion of hMSCs

Simulation type	Bioreactor system	Title	Ref.
Single-phase (<i>RANS</i>)	ambr 15	“The physical characterisation of a microscale parallel bioreactor platform with an industrial CHO cell line expressing an IgG4” and “Agitation conditions for the culture and detachment of hMSCs from microcarriers in multiple bioreactor platforms”	[71, 84]
	125 mL Corning spinner	“Fluid flow and cell proliferation of mesenchymal adipose-derived stem cells in small-scale, stirred, single-use bioreactors”	[50]
	125 mL Corning spinner	“Characterisation of stresses on microcarriers in stirred bioreactor”	[77]
	UniVessel SU 2L and BIOSTAT STR 50L	“Scale-up of adipose tissue-derived mesenchymal stem cell production in stirred single-use bioreactors under low-serum conditions”	[62]
Single-phase (<i>LES</i>)	250 mL mini bioreactor	“Large-Eddy Simulations of microcarrier exposure to potentially damaging eddies inside mini-bioreactors”	[85]
Multi-phase (<i>Euler-Euler</i>)	125 mL Corning spinner	“Fluid flow and cell proliferation of mesenchymal adipose-derived stem cells in small-scale, stirred, single-use bioreactors”	[50]
	UniVessel SU 2L	“Modification and qualification of a stirred single-use bioreactor for the improved expansion of human mesenchymal stem cells at benchtop scale”	[74]
	1.12 L HSB bioreactor	“Revisiting the determination of hydromechanical stresses encountered by microcarriers in stem cell culture bioreactors”	[81]
Multi-phase (<i>Euler-Lagrange</i>)	125/500 mL Corning spinner	“Growth behavior of human adipose tissue-derived stromal/stem cells at small scale: Numerical and experimental investigations”	[12]
	125 mL Corning spinner	“Fluid flow and stresses on microcarriers in spinner flask bioreactors”	[82]
	20L RB bioreactor	“Euler–Lagrange approach to model heterogeneities in stirred tank bioreactors – comparison to experimental flow characterization and particle tracking”	[83]

3.2 Advanced Fluid Flow Characterization of Small-Scale Spinner Flasks: A Case Study

In recent years, various publications in the scientific literature have demonstrated the applicability of stirred SU bioreactors for the *in vitro* expansion of hMSCs. However, the *in vitro* expansion processes that provide clinically relevant cell numbers were developed with cell culture media containing 10–20% FBS. The FBS made the

cells more robust and protected against the various stresses (e.g., hydrodynamic stresses, physiochemical stresses, etc.) that occur during the in vitro expansion [86–88]. The focus of this case study is on the biochemical engineering characterization of the Corning spinner flasks (SP100 and SP300) with numerical methods (single- and multi-phase CFD simulations). Special emphasis is placed on the suspension criteria (N_{slu} and N_{sl}) which are investigated for their use in MC-based hMSC expansions. The case study aims to highlight the use of CFD for the prediction of biochemical engineering parameters and the establishment of a “Digital Twin” to replicate real cultivation systems in silico. For this purpose, multi-phase simulations with a continuum and discrete particle approach were performed, and time-dependent hydrodynamic stresses were derived, based on the transient fluid flow.

3.2.1 Reactor Geometries and Model Approaches

The disposable Corning® spinner flasks (Corning, USA) were commercially available in two different sizes (125 and 500 mL; see Fig. 4). The rigid culture containers were made from polycarbonate and were delivered pre-sterilized. The spinner flasks were equipped with two angled side ports and a 70 mm or 100 mm top cap. The side ports were used for gas exchange (O_2 , CO_2) in a standard cell culture incubator.

The main geometrical features of the two spinner flasks are summarized in Table 6. For all numerical investigations, the working volumes were 100 mL (SP100) and 300 mL (SP300), resulting in H_L/D ratios of 0.64 and 0.60, respectively. Both spinner flasks were equipped with a paddle-like impeller consisting of a blade and a magnetic bar. The impellers were directly mounted on the vessel lid and were magnetically driven.

The fluid domain was modelled based on the geometrical data. Subdomains were defined around the impellers in order to implement the impeller rotation using a *Moving Reference Frame* (MRF) or *Sliding Mesh* (SM) approach. In general, unstructured meshes consisting of tetrahedral elements (SP100 = 712,060 CV,

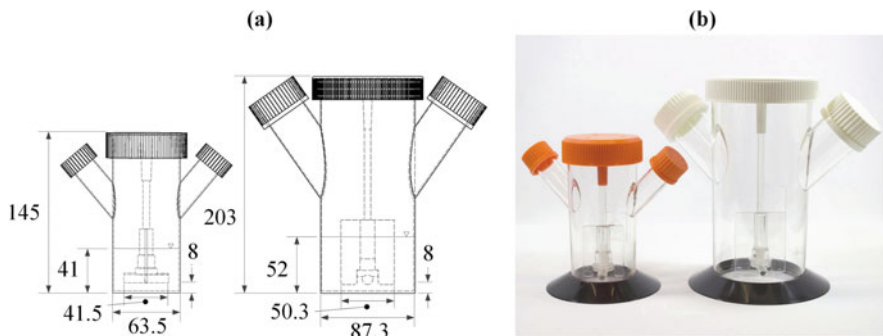


Fig. 4 Small-scale SU Corning spinner flasks (125 and 500 mL) [89]. (a) Technical drawings with the main geometrical dimensions (mm). (b) Picture of the spinner flasks

Table 6 Overview of main geometrical features of the two Corning spinner flasks

		125 mL Corning spinner (SP100)	500 mL Corning spinner (SP300)
V_{min}	mL	25	50
V_{max}	mL	100	300
D_R	mm	64	87
$H_{L,max}$	mm	41	52
d_R	mm	41	50
h_R	mm	8	8
H_L/D_R	–	0.65	0.60
d_R/D_R	–	0.65	0.58
h_R/D_R	–	0.13	0.09

SP300 = 2,073,079 CV) were used. In addition, a boundary layer along the vessel walls was implemented to improve the resolution of effects close to the vessel walls. The CFD simulations were performed using the *ANSYS Fluent* finite volume solver. The implemented pressure-based solver, with an absolute velocity formulation, was used for all simulations. The walls were treated as non-slip boundaries with standard wall functions. The liquid surfaces were treated as symmetry planes, with the fluid velocities normal to the face set to zero. The MCs were implemented in the simulations using (I) a *Euler-Euler granular* model or (II) a *Euler-Lagrange* approach with discrete particle modelling and tracking. In general, water ($\rho_L = 993 \text{ kg/m}^3$, $\eta_L = 0.6913 \text{ mPa s}$ at 37°C) and the MC beads ($d_{p,mean} = 169 \text{ }\mu\text{m}$, $\rho_p = 1,026 \text{ kg/m}^3$) were considered in the models. The initialization of the MCs was carried out either with settled beads (directly at the reactor bottom α_{MC} up to 0.63) or with beads that were homogenously distributed over the entire fluid domain. SIMPLE (semi-implicit method for pressure-linked equations) and phase-coupled SIMPLE algorithms were used for pressure-velocity coupling in the single- and multi-phase models. All simulations were run in parallel and solved on a computational cluster (up to 16 Intel Xeno[®] E5-2630 v4 CPU's @ 2.2 GHz, 64 GB RAM).

3.2.2 Results from Single-Phase Modelling

As shown in Fig. 5a, b, the steady-state fluid flow profiles in the two spinner flask types were similar due to their comparable geometrical ratios. In both cases, the highest fluid velocities occurred at the edges of the impeller blades and in the impeller wake. The maximum fluid velocities were slightly higher ($\leq 5\%$) than the theoretical u_{tip} , which could mainly be attributed to numerical uncertainties. However, the observations are in agreement with literature data for disk stirrers. For example, Stoots et al. [90] and Wollny [91] demonstrated that the peak tangential velocities in the impeller wake can be up to ≈ 1.4 (experimental) and ≈ 1.5 (numeric) times higher than the impeller speed. An area with relatively weak fluid velocities ($u/u_{tip} < 0.1$) was generated directly below the impeller ($r/R \pm 0.3$) in both systems. Thus, this area represented a critical zone for MC sedimentation. The

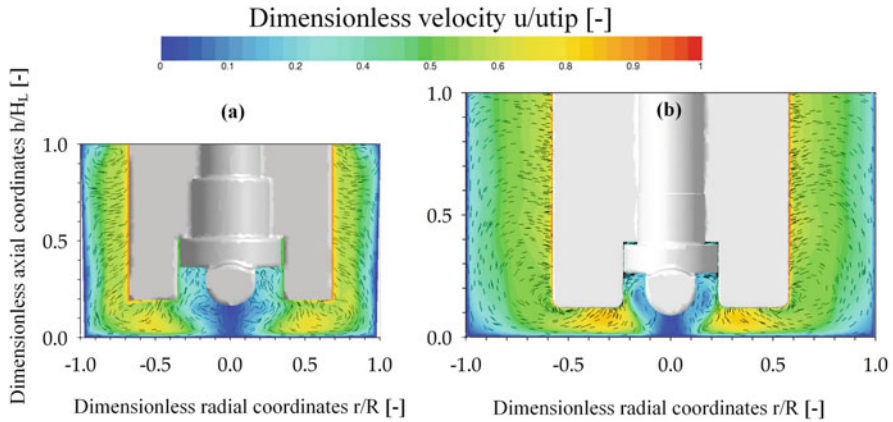


Fig. 5 Steady-state fluid flow inside the SP100 and SP300 [89]. The fluid flow pattern is presented in the vertical mid-plane for N_{stu} -criterion (SP100 = 49 rpm (a), SP300 = 41 rpm (b)) as a combined vector and contour plot

observed MC transport from the outer part of the vessel to the vessel center was mainly driven by the induced secondary flow. Similar findings were also reported by Berry et al. [77], Liovic et al. [82], and Venkat et al. [92] in other types of small-scale spinner flasks.

In addition to the stationary fluid flow, the time-dependent behavior of the fluid velocities was simulated for both systems. Compared to the stationary flow field, the occurrence of vortices at the back of the impeller blades becomes visible. According to the definition of turbulence, these vortices occur stochastically and follow the main fluid flow convectively. Similar findings were also reported by Ismadi et al. [93] by means of PIV measurements of small-scale spinner flasks with a slightly different impeller geometry ($d_R/D = 0.88$). The fluctuations in the fluid velocities also become visible when analyzing the fluid velocities at different positions near the impeller (see Fig. 6). It is obvious that after a certain number of stirrer rotations, a “quasi-periodic” fluid movement was obtained. However, the fluctuations in the lower part of the vessel were higher compared to those near the fluid surface. This was not surprising because of the location of the impeller bar which periodically crossed the different areas. Thus, higher fluid velocity gradients occurred in the lower part of the spinner flasks and increased the local turbulences. However, depending on the strength of the velocity gradients, an effect on the cells may be possible. Berry et al. [77] showed that higher fluid velocity fluctuations can result in local hydrodynamic stresses (10^{-3} to 10^{-1} Pa) for the cells in small-scale spinner flasks which are up to three times higher.

Since a number of mathematical assumptions were used for the CFD modelling, stereoscopic PIV measurements were performed to verify the CFD-predicted fluid flow pattern (see Fig. 7). A detailed description of the experimental setup and procedure for stereoscopic PIV measurements can be found in Jossen et al. [12]. For a quantitative comparison of the individual velocity components, the

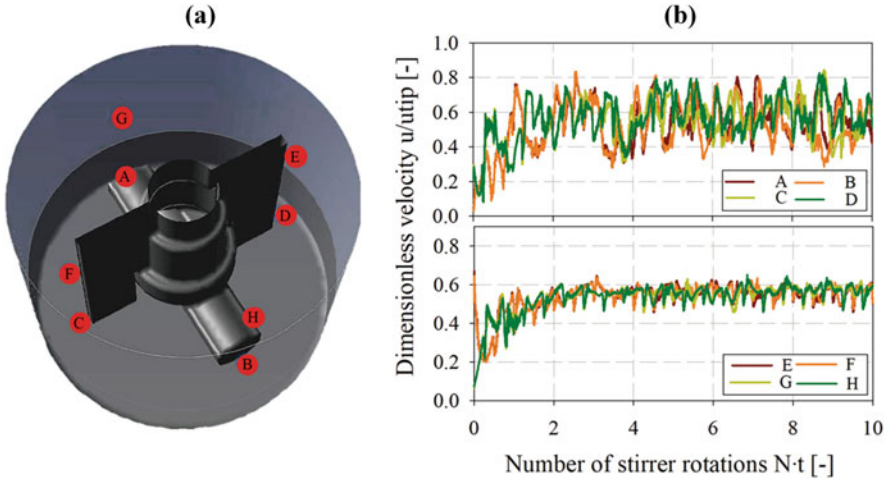


Fig. 6 Time-dependent courses of the fluid velocities at eight different locations within the SP100 [89]. (a) Schematic representation of the different locations within the SP100 (= 49 rpm N_{s1u}). (b) Dimensionless fluid velocity at the different positions during stirrer rotation

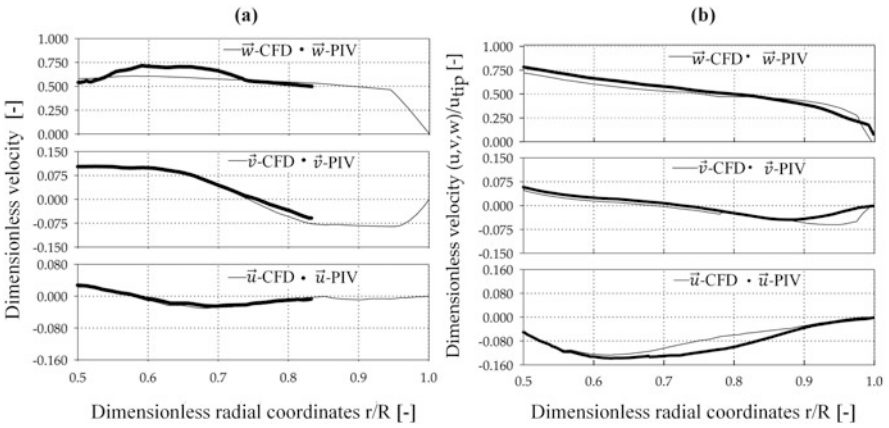


Fig. 7 CFD model verification by experimental PIV measurements in the SP100 and SP300 [89]. Quantitative comparison of CFD-predicted and PIV-measured fluid velocity components (\vec{u} , \vec{v} , \vec{w}) in the SP100 (a) and SP300 (b)

CFD-predicted and PIV-measured data were compared along dimensionless radial coordinates ($0.5-1.0 r/R$) at an axial position of $h/H_L = 0.1$. The comparison of the velocity components in the SP100 revealed only minor differences for \vec{v} (up to 7.5%) and \vec{w} (up to 8.7%). However, the CFD velocity profiles were well captured, and the overall agreement of PIV and CFD was satisfactory, with findings consistent with those of Kaiser et al. [50]. A comparison of the fluid velocities in the SP100 was

only possible for r/R between 0.50 and 0.82 due to the pronounced curve of the vessel surface. The differences between CFD and PIV can be accounted for by measurement uncertainties based on optical phenomena (light refraction and distortion) and the restricted measurement accuracy directly at the edges of the impeller bar (pixel resolution of the camera chip). Thus, direct comparison to the fluid velocities in direct proximity to the impeller is difficult. All three velocity components in the SP300 were well captured by the PIV measurements. The greatest differences (7.9–15%) were found for \bar{u} between r/R 0.70 and 0.85. Hence, it can be concluded that the single-phase CFD model provides reliable fluid flow predictions in both spinner flask types.

3.2.3 Results from Multi-phase Modelling

Oxygen Mass Transfer

Oxygen represents a critical parameter in the cultivation of human cells because it is essential for mitochondrial respiration and oxidative phosphorylation. Hence, the determination of the oxygen mass transfer (OTR) represents an important aspect. However, many of the small-scale bioreactor systems frequently used for the expansion of hMSCs are not equipped with oxygen sensors, which makes it impossible to experimentally determine the oxygen transfer. In such cases, multi-phase CFD simulations can be used to estimate the oxygen mass transfer coefficient (k_{La}), which is shown in the following representative for the SP100.

The multi-phase VOF approach, which takes the headspace into account, was used for the prediction of the k_{La} in the spinner flasks. Figure 8 (a) shows the stationary fluid flow pattern ($N = 49$ rpm) obtained from the multi-phase VOF model, without significant differences to that derived from the single-phase simulations (see Sect. 3.2.2). This conformity between the single and multi-phase simulations was due to the fact that the transport equations for mass and momentum were corrected only at the phase boundary where both the liquid and the gaseous phase were within the control volume. Since only low impeller speeds (≤ 120 rpm) were used in the SP100, marginal changes in the fluid surface with relative low interactions between the liquid and gaseous phases occurred. As a result, the multi-phase VOF model also provided reliable predictions for the fluid flow as well as the fluid surface.

The calculation of the k_{La} value by means of CFD is usually performed in surface-aerated systems using Higbie's penetration model. In this approach, the mass transport is modelled by surface renewal, whereby a characteristic contact time between fluid elements and the phase boundary is calculated (see Eq. (3)).

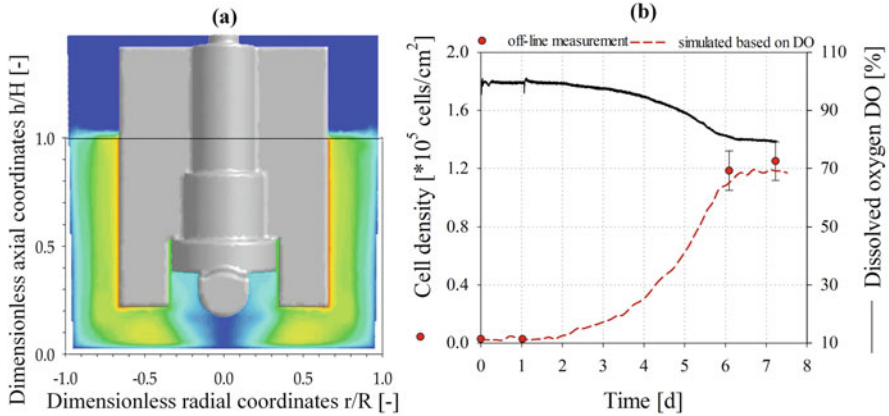


Fig. 8 Fluid flow pattern (a) derived from multi-phase CFD simulation and simulated cell growth (q_{O_2}) based on data from CFD simulation (b)

$$k_L = 2 \cdot \sqrt{\frac{D_{O_2}}{\pi \cdot t_c}} \quad (3)$$

Since the fluid flow in the SP100 was mainly tangentially oriented, the contact time was calculated based on the sum of the fluid velocities (w/o the axial component \vec{v}) and the mean perimeter of the vessel (see Eq. (4)).

$$t_c = \frac{\pi \cdot d_R}{\sqrt{u^2 + w^2}} \quad (4)$$

The specific interface area (a) was defined according to Zhang et al. [94] as the area with a liquid volume fraction of $\alpha_L = 0.5$ divided by the total liquid volume (see Eq. (5)).

$$a = \frac{A_{\alpha_L=0.5}}{V_L} \quad (5)$$

Using this model approach, $k_L a$ values of between 2.6 and 4.2 h^{-1} were predicted for impeller speeds between 49 and 120 rpm ($= u_{tip}$ 0.10–0.26 m/s). Compared to experimentally measured $k_L a$ values (2.6–4.3 h^{-1}), which were measured in a SP100 specially equipped with an optical pO_2 sensor, only minor differences were found. Consequently, the multi-phase CFD model provided reliable predictions about the oxygen mass transfer in the spinner flasks, especially due to the moderate fluid flow conditions and the surface aeration.

Under consideration of the specific oxygen consumption rate ($0.22\text{--}2.5 \times 10^{-17}$ mol/cell/s [89, 95, 96]) or a corresponding yield coefficient for

hMSCs in combination with the oxygen mass transfer, cell growth can be calculated based on the oxygen consumption during the hMSC expansion process (see Eq. (6)).

$$\frac{dX_{MC}}{dt} = k_L a (c_{O_2}^* - c_{O_2}) \cdot Y_{X/O_2} \quad (6)$$

An example of such an oxygen-dependent growth simulation, which was performed with MATLAB, is shown in Fig. 8b. It is recognizable that the cell density can be simulated based on the current oxygen concentration in the SP100 with a satisfactory accuracy. A good correlation (RMSD = 0.05) was obtained between the simulated and the experimental cell density which was measured offline at the beginning and end of the cultivation.

Microcarrier Distribution Based on a *Euler-Euler Granular* Approach

In MC-based hMSC expansion processes, the sufficient suspension of the MCs is an important aspect since a fully suspended state is desired [96–98]. However, since hMSCs are sensitive to hydrodynamic stresses [99–105], the impeller speed and corresponding power input are limited to a certain level, depending on the MC concentration. Therefore, the characterization of the MC-distribution and the derivation of the acting hydrodynamic stresses are important. One possible numeric approach to obtain these data is the use of a *Euler-Euler granular* model in which the two phases are considered as interpenetrating continua. Therefore, mass and momentum are treated individually for each phase. Figure 9 shows an example of the volume-weighted frequency distribution of the dimensionless MC solid fractions (α/α_{mean}) in the two spinner flasks for a MC solid fraction of 0.1% and for the suspension criterion N_{s1u} (SP100 = 49 rpm, SP300 = 41 rpm). As expected, the highest MC volume fractions were, in both cases, found directly below the impeller in the weak mixing zone ($r/R \pm 0.3$; see also Sect. 3.2.2). This observation is not surprising because of the definition of the N_{s1u} . The spatial position of the CFD-predicted deposits agreed well with those made by Kaiser et al. [50]. They also showed a good correlation of their data with experimental observations, which demonstrates the applicability of the *Euler-Euler granular* model for the prediction of the MC distribution in bioreactors. The CFD-derived volume-weighted frequency distribution of the dimensionless MC volume fractions showed comparable MC homogeneity for the two spinner flask types (see Fig. 9c). The fronting of the distributions clearly indicates zones with low MC volume fractions. These zones were mainly determined near the fluid surface, representing the sedimentation boundary. The similar conditions at the vessel bottom can mainly be explained by the same off-bottom clearance ($h_R = 8$ mm), whereas the MC distribution over the entire vessel volume is mostly affected by the d_R/D ratio. The results from the two spinner flasks demonstrate that the *Euler-Euler granular* model provides reliable predictions for MC distribution. However, due to the continuum formulation of the

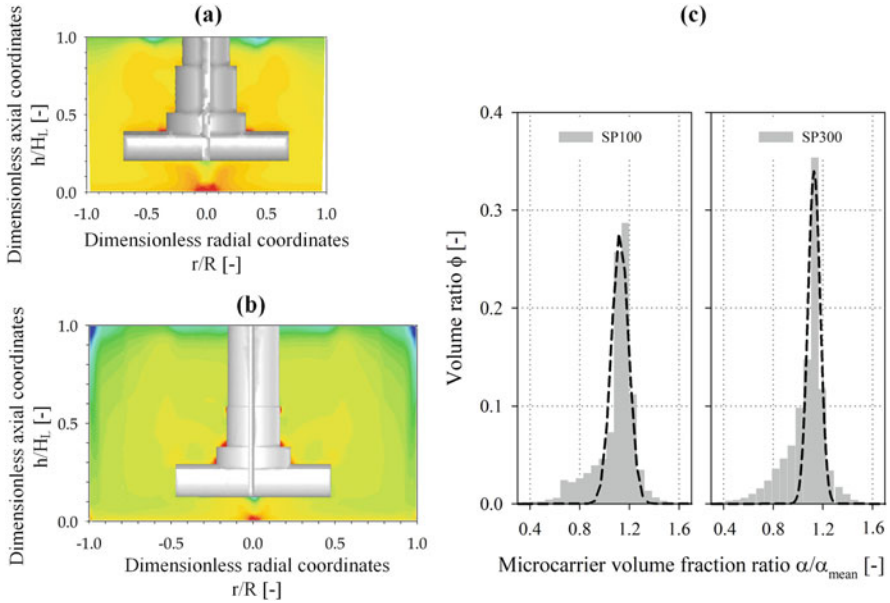


Fig. 9 Contour plots of the dimensionless MC volume fraction (a, b) and volume-weighted frequency distribution (c) at N_{slu} (SP100 = 49 rpm, SP300 = 41 rpm)

model, information on individual particles and their circulation and residence times in different high shear zones cannot be obtained.

Microcarrier Tracking Based on a *Euler-Lagrange* Approach

Euler-Lagrange simulations allow the spatial distribution of discrete MC particles to be derived. Based on this information, the circulation time ($t_{\text{cir.}}$), the residence time ($t_{\text{res.}}$), and the hydrodynamic stresses acting on the particles can be calculated. Data from such an *Euler-Lagrange* simulation is shown representatively in the following figure for the SP100. Figure 10a, b shows an example of the fluctuating forces acting on individual MCs during impeller motion. It is obvious that the acting forces fluctuated in the order of 100. Thus, each particle has its own history in terms of hydrodynamic stress, which means that some particles are exposed to a certain hydrodynamic stress level longer and/or more often than others. Compared to the *Euler-Euler granular* approach, which allows volume-weighted data to be derived, the *Euler-Lagrange* approach gives a discrete description per MC.

The particle data can further be processed to derive the force distribution for specific locations or to calculate the circulation and residence times. For this purpose, the two spinner flask types were vertically divided into four zones ($\Delta h/H_L \approx 0.25$). Figure 11 exemplifies the SP100, showing the force distribution in the four defined spinner segments. It is obvious that logarithmic normal distributions

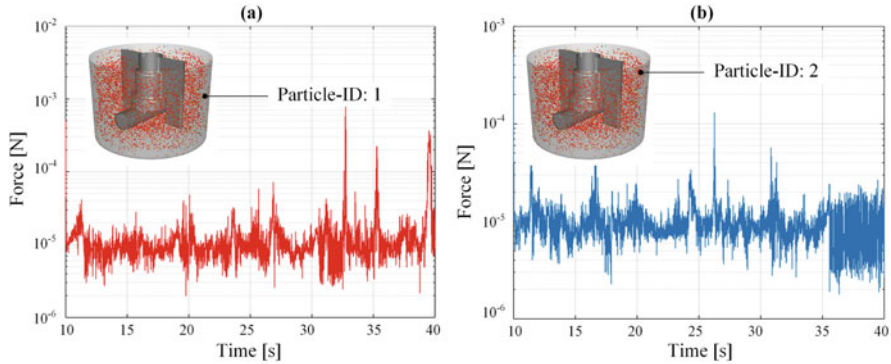


Fig. 10 Force acting on the MCs during the impeller motion. Time-dependent force diagrams are shown representatively for two individual particles in the SP100 ($N = 49$ rpm)

were obtained where highest forces occurred in the lowest segment. Thus, cells on MCs were more stressed in the lowest spinner segment. This observation was also supported by the fact that the highest probability of the presence of MCs was in the lowest spinner segment. However, the effects of the hydrodynamic stresses in the different zones depended heavily on the particle circulation and residence times, demonstrating the dynamics and complexity of the systems. For this reason, circulation times and residence times were calculated for each individual spinner segment based on the particle tracking data and were subsequently averaged over the four segments (see Table 7). As expected, the circulation times (2.7–11.5 s) decreased proportionally to the residence times (0.74–4.94 s) as the impeller speed was increased. Interestingly, the proportionality constants for the SP100 ($= 0.54$) and the SP300 ($= 0.49$) were quite similar. This observation can be ascribed to the comparable fluid flow conditions. The calculated mean forces were inversely proportional to the circulation and residence times. This finding is not unexpected since the specific power input, which can be calculated based on the torque acting on the impeller during the CFD simulation, increased by approximately the 3rd power in both spinner flask types. Interestingly, the mean values of particle forces did not change significantly between the lower impeller speeds ($N < N_{slu}$) and the two suspension criteria, even though the circulation and residence times decreased by up to 50%. Impeller speeds exceeding N_{slu} and N_{sl} resulted in a slight decrease of the circulation times, although the related particle forces increased by exponents of 0.07–0.12 in respect of the resulting specific power input.

Comparable observations for the specific power input are also possible when considering the local normal and shear stresses, which can be calculated according to Wollny [91]. The volume-weighted mean values of the local normal and shear stresses were in a comparable range in both spinner flask types for impeller speeds between N_{slu} and N_{sl} . Consequently, comparable conditions in terms of hydrodynamic stresses can be expected for cultivations in the resulting specific power input range of 0.3–1.1 W/m^3 . Another popular method for evaluating hydrodynamic stress

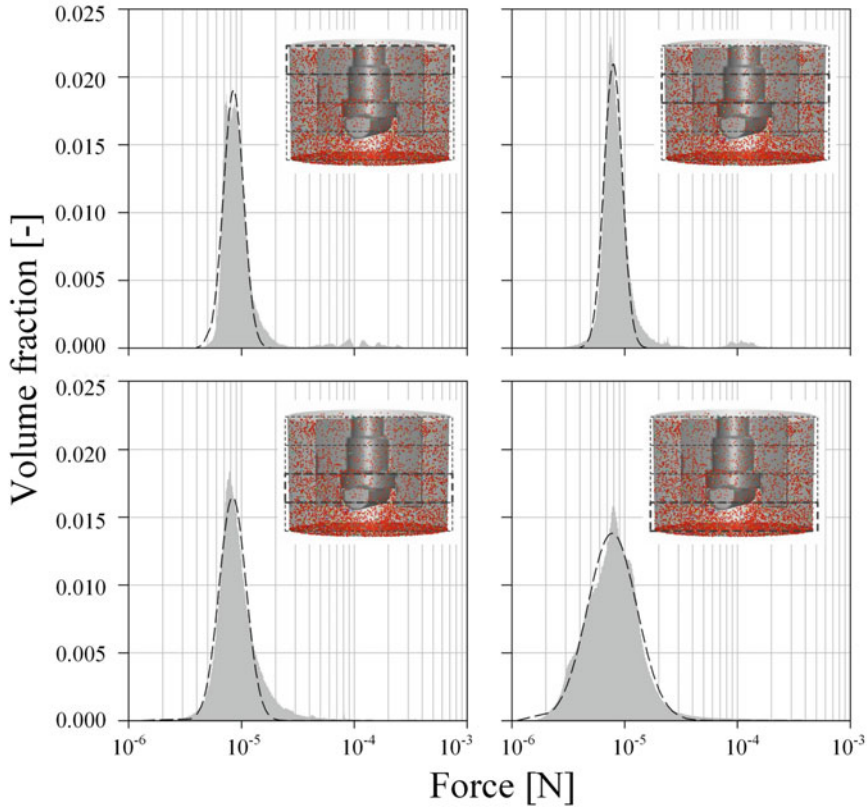


Fig. 11 Force distributions in the different spinner segments

is based on the Kolmogorov length scale, which can be calculated from CFD simulations. While cells in suspension are assumed to only be affected by turbulent eddies of comparable size, those growing on the surface of an MC appear to be more shear sensitive. Croughan et al. [106] found that cell damage became significant when the smallest turbulent eddies were approximately two-thirds of the size of an MC. However, to apply Kolmogorov's theory, the fluid flow must be very turbulent ($Re > 10^4$). The flow in the two-spinner flasks can be described as moderately turbulent. However, the calculated maximum dissipation rates were higher by a factor of two in the impeller swept volume than in the bulk. As expected, the smallest turbulent eddies were found for the highest tested impeller speeds, with values between 30 and 47 μm . In terms of the suspension criteria, the minimum values were predicted between 60 and 76 μm , which is much lower than the proposed two-thirds MC size. In contrast, the volume-weighted mean values were slightly higher than the MC size, which demonstrated that only a small proportion of the turbulent eddies are comparable in size to the MCs. This lowers the risk that the MCs might come into contact with these detrimental eddies. However, this fact also

Table 7 Overview of the main biochemical engineering parameters derived from the CFD simulations

N [rpm]	u_{tip} [m/s]	Re	P/V [W/m ³]	$t_{cir.}$ [s]	$t_{res.}$ [s]	$l_{\lambda}^{(a)}$ [μ m]	$\tau_{nl}^{(b)}$ [10 ⁻³ Pa]	$\tau_{nn}^{(b)}$ [10 ⁻³ Pa]	$F^{(c)}$ [10 ⁻⁵ N]
<i>Corning 125 mL spinner (SP100)</i>									
25	0.05	715	0.07	11.5	4.9	130/ 530	2.72/79	0.79/43	0.75
49 N_{s1u}	0.11	1,402	0.63	6.5	2.4	66/ 228	5.39/169	1.15/108	0.85
60 N_{s1}	0.13	1,717	1.12	6.0	1.9	60/ 191	6.62/211	1.32/138	0.91
120	0.26	3,434	7.56	4.0	0.9	30/ 111	12.91/437	2.24/301	1.82
<i>Corning 500 mL spinner (SP300)</i>									
20	0.05	841	0.05	10.0	4.2	136/ 546	2.04/214	0.30/138	0.83
41 N_{s1u}	0.11	1,724	0.33	6.2	2.6	76/ 295	4.00/481	0.69/362	0.89
52 N_{s1}	0.14	2,186	0.61	5.9	1.6	66/ 282	5.00/679	0.87/473	1.04
100	0.26	4,204	3.70	2.7	0.7	47/ 181	9.26/ 1,350	1.70/872	2.10

^aVolume -weighted minimum/mean values of turbulent Kolmogorov length scale

^bLocal shear (τ_{nl}) and normal (τ_{nn}) stress for volume-weighted mean/maximum values

^cMean values of acting particle force weighted by number

depends heavily on the resulting circulation and residence times of the MCs. In both cases, the mean volume-weighted values for the highest tested impeller speeds were much closer to the detrimental theoretical value of 141 μ m. Even though such eddies occurred at the suspension criteria, the frequency with which the MCs were exposed to such eddies was much lower due to the lower circulation times and residence times.

3.2.4 Linking of CFD-Derived Data with Cultivation Studies

In order to link the CFD-derived engineering data with cell biological aspects, cultivation studies in the two spinner flask types at different impeller speeds were performed. The results of the cultivation studies with hMSCs from the adipose tissue are summarized in Table 8. It is obvious that the different hydrodynamic stress levels have a significant effect on the cell growth in both spinner flask types. Highest living cell densities were achieved, of up to $1.68 \pm 0.36 \times 10^5$ cells/cm² ($= 6.25 \pm 0.35 \times 10^5$ cells/mL, EF 56) and $2.46 \pm 0.16 \times 10^5$ cells/cm² ($= 8.77 \pm 0.66 \times 10^5$ cells/mL, EF 81), in the SP100 and SP300 when working at $N_{s1u} \leq N \leq N_{s1}$ (SP100 = 49–63 rpm, SP300 = 41–52 rpm). The peak living cell densities in the SP300 were on average up to 40% higher than those in the SP100. Although the two spinner

Table 8 Summary of cultivation results with hMSCs from the adipose tissue in the SP100 and SP300

N [rpm]	Living X_{max} [10^5 cells/cm ²]	EF	μ [d ⁻¹]	t_d [d]	q_{Glc} [pmol/ cell/d]	q_{Lac} [pmol/ cell/d]	q_{Amm} [pmol/ cell/d]
<i>Corning 125 mL spinner (SP100)</i>							
25	1.05 ± 0.06	35.0	0.6 ± 0.0	1.1 ± 0.1	13.2 ± 2.3	20.7 ± 2.7	8.8 ± 0.3
49 N_{sLu}	1.67 ± 0.12	55.6	0.7 ± 0.0	1.0 ± 0.0	10.6 ± 1.6	35.2 ± 1.9	6.1 ± 0.4
60 N_{sI}	1.68 ± 0.36	56.0	0.7 ± 0.1	0.9 ± 0.1	9.8 ± 0.8	30.3 ± 1.0	6.2 ± 0.3
120	0.60 ± 0.04	20.1	0.5 ± 0.1	1.5 ± 0.4	35.0 ± 1.6	88.8 ± 5.2	16.5 ± 0.3
<i>Corning 500 mL spinner (SP300)</i>							
20	1.36 ± 0.57	45.2	0.5 ± 0.1	1.3 ± 0.1	21.0 ± 0.9	28.6 ± 9.9	14.7 ± 0.2
41 N_{sLu}	2.46 ± 0.16	81.9	0.7 ± 0.0	1.0 ± 0.0	15.5 ± 0.6	40.6 ± 1.8	10.6 ± 0.5
52 N_{sI}	2.43 ± 0.66	81.1	0.7 ± 0.0	1.0 ± 0.0	11.8 ± 1.2	35.3 ± 3.3	9.7 ± 0.4
100	1.25 ± 0.29	41.8	0.5 ± 0.1	1.3 ± 0.0	20.8 ± 9.8	88.6 ± 2.1	19.0 ± 1.4

flask types had comparable geometrical ratios, the hydrodynamic stresses in the SP100 were higher at the suspension criteria. In fact, the absolute hydrodynamic stresses over time were higher due to the lower circulation times, which increase the risk that the cells on the MCs are more frequently exposed to detrimental stresses. At the same time, the residence times, and therefore also the exposure times, of the MCs to the hydrodynamic stresses were shorter, as the multi-phase simulations have indicated. In both cases, the peak cell densities were in the same range as cell densities measured in planar static cultures at maximum confluency ($\approx 2.9 \times 10^5$ cells/cm²), in which the cells were expanded in parallel. This result indicates that the cells cultivated at $N_{sLu} \leq N \leq N_{sI}$ are mainly restricted by the available growth surface. In contrast, significant lower cell densities were achieved at lower and higher impeller speeds. A peak living cell density of $1.05 \pm 0.06 \times 10^5$ cells/cm² ($= 4.49 \pm 0.06 \times 10^5$ cells/mL, EF 35) and $1.36 \pm 0.57 \times 10^5$ cells/cm² ($= 4.48 \pm 0.57 \times 10^5$ cells/mL, EF 45) was determined for the SP100 and SP300 at 25 rpm and 20 rpm, respectively. These peak cell densities are up to 84% lower than those at $N_{sLu} \leq N \leq N_{sI}$. This observation may have been caused by the higher amount of sedimented MCs and the increased MC-cell aggregate formation (see also [12]). The viability of the cells on the MCs was always >99%. This was not surprising as dead cells detach from the MC surface. Thus, the increase in dead cells in the supernatant depends on the cell detachment from the MC surface and the die-off of cell in the supernatant.

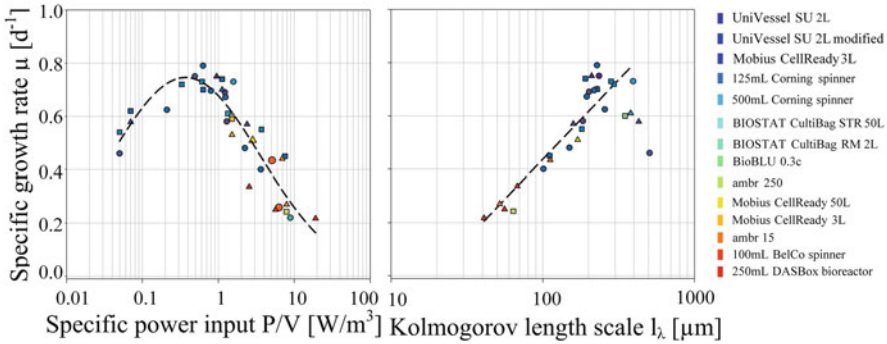


Fig. 12 Dependency of the specific growth rate on the CFD-derived specific power input (a) and the Kolmogorov length scale (b) [89]. Data from other SU bioreactors were obtained from the literature: UniVessel SU 2L [62, 74], UniVessel SU 2L modified [74], Mobius CellReady 3L [89, 108], BIOSTAT STR 50 L [62, 89], BIOSTAT RM 2L [11], Mobius CellReady 3L [63], ambr 15 [109], 100 mL BellCo spinner [109], 250 mL DASbox bioreactor [73]

By considering q_{Glc} , it becomes clear that the lowest values were obtained for impeller speeds in the range of $N_{s1u} \leq N \leq N_{s1}$ in both cases. This is due to the efficient metabolization of glucose under these hydrodynamic conditions. The calculated values for the hMSCs correspond to those determined by Rafiq et al. [54] and Heathmann et al. [107] in different cell culture media. The highest q_{Glc} (21–35 pmol/cell/d) were found at the highest impeller speeds. The relationship between the q_{Glc} and the specific power input can be expressed by a statistical, logarithmic function of 3rd order. Similar correlations were also found for q_{Lac} and q_{Amm} . However, such statistical correlations are only valid for the investigated P/V range. Values of up to 193% and 170% higher than those in the spinner flasks at N_{s1u} and N_{s1} were determined for q_{Lac} and q_{Amm} at the highest impeller speeds. These higher values indicated that the cells are more stressed at higher impeller speeds as a result of the higher hydrodynamic stresses. The different correlations obtained were used as initial parameters for the cell growth modelling (see Sect. 4.2).

Figure 12a, b shows the relationship between the overall mean specific growth rate and the specific power input and Kolmogorov length scale, respectively. The parabolic curve profile of the specific growth rate shows optimal cell growth for $N_{s1u} \leq N \leq N_{s1}$. For specific power inputs between 0.33 and 1.12 W/m^3 , maximum μ between 0.70 and 0.74 d^{-1} were achieved. This function also correlates well with literature data from other SU bioreactors. Similar relationships to the specific power input were also established for the Kolmogorov length scale, where a linear relation was found. Thus, CFD-derived hydrodynamic stress data can be used to find correlations between biochemical engineering and cell cultivation aspects and to define optimum cultivation conditions for MC-based hMSC expansion processes.

4 Mathematical Growth Modelling of MC-Based hMSC Expansions

The development of mathematical growth models to describe or predict hMSC growth is gaining in importance. This is not surprising since the cell material is often limited and isolated directly from the patient. Thus, the prediction of the cell growth depending on patient data (e.g., age, health status) is an important aspect, especially for autologous therapies. The following section gives a brief overview of different growth models described in the literature for the expansion of hMSCs. In addition, a case study is presented and discussed, which presents an unstructured, segregated growth model for the expansion of hMSCs on MCs.

4.1 Modelling Approaches

Table 9 gives an overview of publications describing different model approaches for the simulation of the hMSC growth. For example, Higuera et al. [110], Dos Santos et al. [111], and Jossen et al. [12] used kinetic growth models based on Monod-type kinetics. Higuera et al. focused in its formulation only on the substrate/metabolite inhibition, whereas Dos Santos and Jossen et al. introduced terms that considered cell contact inhibition. All models allowed the hMSC cell growth and substrate

Table 9 Overview of hMSC growth models described in the literature

Model type	Title	Ref.
Monod-type kinetic models	“Quantifying in vitro growth and metabolism kinetics of human mesenchymal stem cells using a mathematical model”	[110]
	“Ex-vivo expansion of human mesenchymal stem cells: a more effective cell proliferation kinetics and metabolism under hypoxia”	[111]
	“Growth behavior of human adipose tissue-derived stromal/stem cells at small scale: numerical and experimental investigations”	[12]
Population balance models	“Population balance modelling of stem cell culture in 3D suspension bioreactors”	[112]
	“Experimental analysis and modelling of bone marrow mesenchymal stem cells proliferation”	[113]
	“A mathematical framework to study the effects of growth factor influences on fracture healing”	[114]
	“Modelling of in vitro mesenchymal stem cell cultivation, chondrogenesis and osteogenesis”	[115]
Cellular automaton models	“Population dynamics of mesenchymal stromal cells during culture expansion”	[116]
	“Expansion of adipose mesenchymal stromal cells is affected by human platelet lysate and plating density”	[117]
Cell-based podia model	“Spatial organization of mesenchymal stem cells in vitro – results from a new individual cell-based model with podia”	[118]

consumption to be described based on the experimental setup investigated. In contrast to the Monod-type models, Bartolini et al. [112], Mancuso et al. [113], Bailon-Plaza et al. [114], and Geris et al. [115] used population balance models. For example, Bailon-Plaza et al. [114] included different cell populations in their model in order to describe not only hMSC proliferation but also chondrogenic and osteogenic differentiation. However, all models included parameters strongly influenced by various biological aspects. A discrete formulation of the cells was given by Schellenberg et al. [116] and Cholewa et al. [117], who both used cellular automaton models to describe the hMSC cell growth. However, these models did not include a metabolic description of substrate consumption and metabolite production, which can have an inhibitory effect on the cell growth. Hoffmann et al. [118] developed an individual cell-based model with podia, which is able to quantitatively describe the spatio-temporal organization of MSC culture. They modelled discrete cells and considered their orientation on a planar surface. Hence, the model considers the effects of contact inhibition and the organization and orientation of the cell monolayer. However, the model does also not reflect the metabolism of different substrates or the production of inhibitory metabolites.

4.2 Kinetic Growth Model for the MC-Based hMSC Expansion: A Case Study

Based on theoretical considerations, an unstructured, segregated, simplistic growth model was developed for the MC-based hMSC expansion in the SP100 and SP300. Theoretically, the entire expansion process can be divided into four steps: (I) cell sedimentation and initial attachment, (II) cell spreading and migration, (III) mitotic cell division, and (IV) cell growth arrest due to contact or substrate inhibition, which partially ran in parallel. The general concept of the growth model and the factors that influence the MC-based culture are shown in Fig. 13. During the cultivation period, the formation of MC-cell aggregates is promoted due to the increasing number of cells per bead and periodic particle interactions. The rate of the MC-cell aggregate formation is influenced by the frequency and strength of the hydrodynamic stresses. However, the rate of MC-cell aggregate formation was not considered in the current version of the MC-based growth model because the aggregation process is very complex and depends on many physical and biological parameters. Due to the fact that hMSC growth is anchorage-dependent, possible formation of spheroids in the suspension was not considered in the model. This simplification was justified since no spheroid formation was observed in the MC-based expansions. Thus, it can be assumed that cells in suspension do not contribute to an increase in the overall cell number, with cell growth restricted to the MC surface. To define the starting conditions, it was assumed that initial cell attachment took place during the cell attachment phase, which can be described by the attachment constant k_{at} . After the cells had attached themselves to the MC surface, a short cell adaption phase was

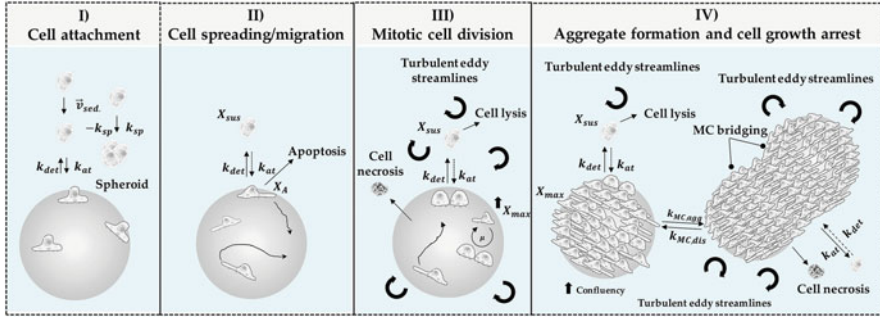


Fig. 13 Schematic representation of different phases and influencing factors during the MC-based expansion of hMSCs. The MC-based expansion can be divided into four phases: (I) cell sedimentation/attachment, (II) cell spreading/migration, (III) mitotic cell division, (IV) MC-cell aggregate formation and cell growth arrest, with some running in parallel

considered before the cells began to proliferate. The cell adaption phase was considered by introducing the coefficient α (see Eq. (7)),

$$\alpha(t) = \frac{t^n}{t_l^n + t^n} \quad (7)$$

where t_l defined the lag time or adaption time and the point at which $\alpha(t)$ is half of the maximum. The exponent n affects the slope of $f(\alpha(t))$. If $n = 1$, $\alpha(t)$ is described by Michaelis-Menten kinetics. Otherwise, a sigmoidal curve is obtained that becomes steeper as n increases. Both variables can be obtained from experimental growth studies.

The specific cell growth rate (μ) was calculated based on Monod-type kinetics. Hence, glucose (Glc), lactate (Lac), ammonium (Amn), and the available growth surface (X_{max}) were considered to be influencing factors (see Eq. (8)). However, investigations indicated that cell growth restriction based on maximum available growth surface does not follow a normal Monod-type kinetic. This fact can mainly be ascribed to cell migration during cell growth. Thus, the effect of the growth surface restriction term becomes more significant towards the end of the cell growth phase. For this reason, the exponent n was also introduced in Eq. (8).

$$\mu = \mu_{max} \cdot \left(\frac{Glc}{K_{Glc} + Glc} \right) \cdot \left(\frac{K_{Lac}}{K_{Lac} + Lac} \right) \cdot \left(\frac{K_{Amn}}{K_{Amn} + Amn} \right) \cdot \left(\frac{X_{max}^n - X_A^n}{X_{max}^n} \right) \quad (8)$$

The cell number on the MC surface (X_A) increased through mitotic cell division and the attachment of cells from the suspension (see Eq. (9)). However, this increase in cell number was affected by the detachment of hMSCs from the planar growth surface, which was accounted for by the detachment constant ($-k_{det}$).

$$\frac{dX_A}{dt} = \alpha \cdot \mu \cdot X_A + k_{at} \cdot \frac{(X_{max}^n - X_A^n)}{X_{max}^n} \cdot X_{Sus} - k_{det} \cdot X_A \quad (9)$$

However, the detachment constant $-k_{det}$ is strongly affected by hydrodynamic forces and is therefore variable for different specific power inputs. As mentioned previously, cell growth in the suspension is negligible, and, therefore, changes in cell concentration will only be affected by attachment to or detachment from the MC surface (see Eq. (10)).

$$\frac{dX_{Sus}}{dt} = k_{det} \cdot X_A - k_{at} \cdot \frac{(X_{max}^n - X_A^n)}{X_{max}^n} \cdot X_{Sus} \quad (10)$$

Contrary to the growth restriction based on the specific growth rate, glucose consumption was only limited by the glucose concentration itself (see Eq. (11)). Consequently, glucose consumption was the result of the glucose uptake by the mitotic cells and the maintenance metabolism of mitotic and non-mitotic cells (X_V). A step response (δ_{Glc}) was implemented in Eq. (11) to avoid negative glucose concentrations.

$$\frac{dGlc}{dt} = -\frac{1}{Y_{\frac{x}{glc}}} \cdot \alpha \cdot \mu \cdot \frac{(X_{max}^n - X_A^n)}{X_{max}^n} \cdot X_A - m_{Glc} \cdot \delta_{Glc} \cdot X_V \quad (11)$$

L-glutamine (*Gln*) consumption was not considered in this model since metabolic measurements from the experiment indicated that *Gln* is not a limiting factor. Moreover, UltraGlutamine (L-alanyl-L-glutamine) is used in most stem cell culture medium for which the model was developed and had undergone a series of complex degradation steps (i.e., (I) cleavage by extracellular peptidases and (II) degradation of free L-glutamine or absorption into the cells and metabolization). The production of lactate (*Lac*) and ammonium (*Amn*) was accounted for by Eqs. (12) and (13).

$$\frac{dLac}{dt} = q_{Lac} \cdot X_A \cdot \alpha + p_{Lac} \cdot X_V \quad (12)$$

$$\frac{dAmn}{dt} = q_{Amn} \cdot X_A \cdot \alpha + p_{Amn} \cdot X_V \quad (13)$$

The validity of the unstructured, segregated growth model was tested for MC-based hMSC expansions in the SP100 and SP300 (each $n = 3$), which were performed at N_{slu} (SP100 = 49 rpm, SP300 = 41 rpm). All growth-related simulations were performed with MATLAB 2019b (MathWorks Inc.) where the model equations were solved using the *ode15s* solver (Intel Core i-7 CPU @ 2.6 GHz, 32 GB RAM). Table 10 shows the parameters and the initial values for the growth simulations which were derived from experimental cultivation studies.

Figure 14 shows the measured values and simulated timelines for the cell density (a, c), as well as the substrate and metabolites (b, d). The simulated timelines show

Table 10 Cell growth-dependent parameters used for the simulations of the MC-based hMSC cell growth in the SP100 and SP300

Parameter		Values	Parameter		Values
μ_{max}	1/d	0.64–0.68	Lac	mmol/L	0.0
Amn	mmol/L	0.0	q_{Amn}	mmol/cell/d	6–19
Glc	mmol/L	30.5	q_{Glc}	mmol/cell/d	9.8–35
k_{at}	1/d	0.4–1.0	q_{Lac}	mmol/cell/d	20–89
k_{det}	1/d	0.003–0.009	t_l	d	1.5–1.9
K_{Amn}	mmol/L	8–10	X_A	cells/mL	0
K_{Glc}	mmol/L	0.4	X_{Sus}	cells/mL	10,800
K_{Lav}	mmol/L	35–50			

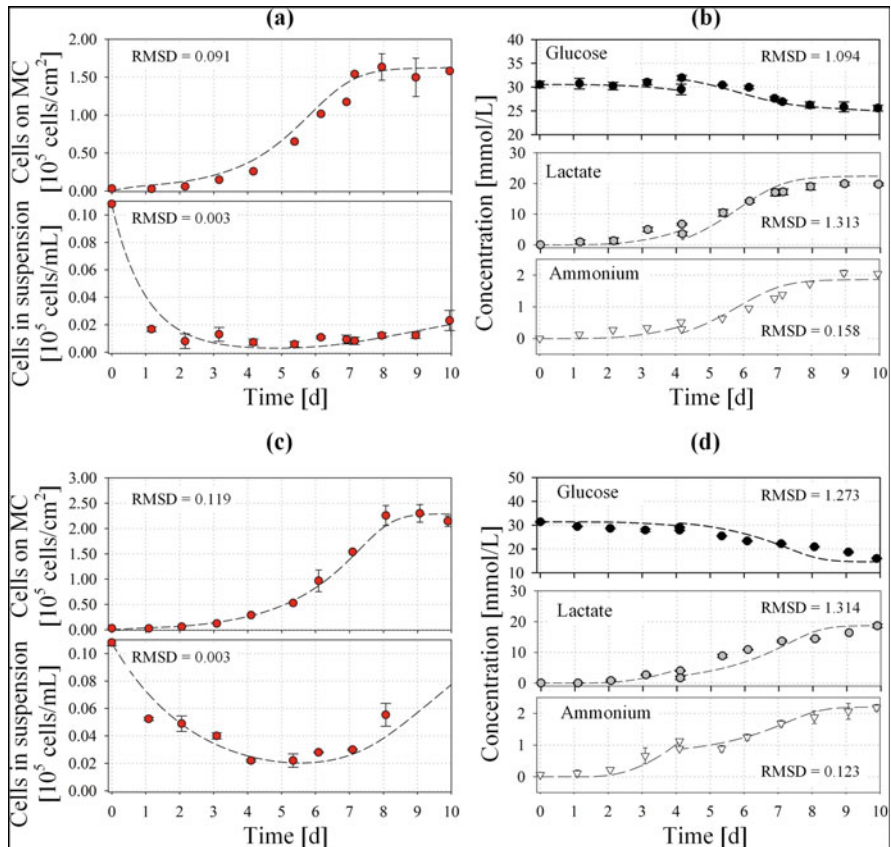


Fig. 14 Comparison of experimental (symbols) and simulated (line) data for cell density (a, c) and substrate/metabolites (b, d). The growth simulations were performed for the SP100 (a, b) and SP300 (c, d)

pleasing overall correlation with the values measured experimentally and demonstrate the applicability of the unstructured, segregated growth model. By using determined growth parameters from cultivation studies, the cell growth, glucose consumption, lactate production, and ammonium production could be proficiently approximated. The greatest deviations in cell density were in the range of 3–20% for the cells in suspension and 4–24% for the cells on the MCs. The glucose, lactate, and ammonium timelines also correspond to this pattern, even though the specific substrate consumption and metabolite production rates were prone to errors. However, the models provide reliable predictions for the MC-based hMSC growth in the two spinner flask types.

5 Conclusions and Outlook

In this review, the current state of the art of the in vitro expansion of hMSC and the use of numerical tools to support the development of MC-based hMSCs expansions as well as the establishment of “Digital Twins” have been presented. It has been emphasized that different CFD model approaches are described in the scientific literature which can be successfully applied for the characterization of SU bioreactors, especially for the process development of hMSC expansion processes. The CFD case study presented clearly demonstrates that numerical models are valuable tools for the biochemical engineering characterization of small-scale spinner flasks, especially for the determination of parameters that are difficult to determine experimentally. A good correlation was always found between the parameters predicted by the CFD and those measured experimentally. This observation was also in agreement with the literature data. The *Euler-Euler* and *Euler-Lagrange* models gave adequate predictions of the MC distributions within the spinner flask systems and were correlated qualitatively with experimental observations. The *Euler-Lagrange* approach allowed the calculation of particle histories due to its discrete particle formulation, which can be combined with experimental cultivation studies. Thus, *Euler-Lagrange* modelling should be favored in the future in order to derive hydrodynamic stresses over time instead of volume-weighted data. The scientific literature summarized also shows that different model approaches for the simulation of the hMSC growth are available, even though only a few are applicable for the MC-based growth simulation in a stirred bioreactor. The unstructured and segregated growth model presented gives a good description of the MC-based hMSC expansion process in the two spinner flask systems. Thus, MC-based hMSC cell growth can be predicted. However, the further development of descriptive, or even predictive, models for hMSCs will be important in the future for exact scheduling of the preparation of the cell material and the subsequent autologous therapy.

References

1. Grand View Research (2020) Cell therapy market size, share and trends analysis report, 2020–2027
2. Malik NN, Durdy MB (2015) Cell therapy landscape. In: Translational regenerative medicine. Elsevier, pp 87–106
3. Simaria AS, Hassan S, Varadaraju H, Rowley J, Warren K, Vanek P, Farid SS (2014) Allogeneic cell therapy bioprocess economics and optimization: single-use cell expansion technologies. *Biotechnol Bioeng* 111:69–83. <https://doi.org/10.1002/bit.25008>
4. Sharma S, Raju R, Sui S, Hu W-S (2011) Stem cell culture engineering – process scale up and beyond. *Biotechnol J* 6:1317–1329. <https://doi.org/10.1002/biot.201000435>
5. Ren G, Chen X, Dong F, Li W (2012) Concise review: mesenchymal stem cells and translational medicine: emerging issues. *Stem Cells Transl Med* 1:51–58
6. Capelli C, Pedrini O, Valgardsdottir R, Da Roit F, Golay J, Introna M (2015) Clinical grade expansion of MSCs. *Immunol Lett* 168:222–227. <https://doi.org/10.1016/j.imlet.2015.06.006>
7. Wagner W, Horn P, Castoldi M, Diehlmann A, Bork S, Saffrich R, Benes V, Blake J, Pfister S, Eckstein V, Ho AD (2008) Replicative senescence of mesenchymal stem cells: a continuous and organized process. *PLoS One* 3:e2213. <https://doi.org/10.1371/journal.pone.0002213>
8. Lo Surdo J, Bauer SR (2012) Quantitative approaches to detect donor and passage differences in adipogenic potential and clonogenicity in human bone marrow-derived mesenchymal stem cells. *Tissue Eng Part C Methods* 18:877–889. <https://doi.org/10.1089/ten.tec.2011.0736>
9. Heathman TRJ, Rafiq QA, Chan AKC, Coopman K, Nienow AW, Kara B, Hewitt CJ (2016) Characterization of human mesenchymal stem cells from multiple donors and the implications for large scale bioprocess development. *Biochem Eng J* 108:14–23. <https://doi.org/10.1016/j.bej.2015.06.018>
10. Das R, Roosloot R, van Pel M, Schepers K, Driessen M, Fibbe WE, de Bruijn JD, Roelofs H (2019) Preparing for cell culture scale-out: establishing parity of bioreactor- and flask-expanded mesenchymal stromal cell cultures. *J Transl Med* 17:241. <https://doi.org/10.1186/s12967-019-1989-x>
11. Jossen V, Schirmer C, Mostafa Sindi D, Eibl R, Kraume M, Pörtner R, Eibl D (2016) Theoretical and practical issues that are relevant when scaling up hMSC microcarrier production processes. *Stem Cells Int* 2016:1–15. <https://doi.org/10.1155/2016/4760414>
12. Jossen V, Eibl R, Kraume M, Eibl D (2018) Growth behavior of human adipose tissue-derived stromal/stem cells at small scale: numerical and experimental investigations. *Bioengineering* 5:106. <https://doi.org/10.3390/bioengineering5040106>
13. Hassan S, Simaria AS, Varadaraju H, Gupta S, Warren K, Farid SS (2015) Allogeneic cell therapy bioprocess economics and optimization: downstream processing decisions. *Regen Med* 10:591–609
14. Lipsitz YY, Milligan WD, Fitzpatrick I, Stalmeijer E, Farid SS, Tan KY, Smith D, Perry R, Carmen J, Chen A, Mooney C, Fink J (2017) A roadmap for cost-of-goods planning to guide economic production of cell therapy products. *Cytotherapy* 19:1383–1391. <https://doi.org/10.1016/j.jcyt.2017.06.009>
15. García-Fernández C, López-Fernández A, Borrós S, Lecina M, Vives J (2020) Strategies for large-scale expansion of clinical-grade human multipotent mesenchymal stromal cells. *Biochem Eng J* 159:107601. <https://doi.org/10.1016/j.bej.2020.107601>
16. Dolley-Sonneville P, Melkounian Z, Romeo L. Corning® Stemgro® hMSC Medium. Corning Appl Note 1–8
17. Gottipamula S, Muttigi MS, Chaansa S, Ashwin KM, Priya N, Kolkundkar U, Sundar Raj S, Sen MA, Seetharam RN (2016) Large-scale expansion of pre-isolated bone marrow mesenchymal stromal cells in serum-free conditions. *J Tissue Eng Regen Med* 10:108–119. <https://doi.org/10.1002/term.1713>

18. Carter SM, Granchelli J, Stelzer T (2014) Large scale expansion and differentiation of human mesenchymal stromal cells in the Thermo Scientific nunc cell factory system. *Thermo Sci Appl Note* 1:1–6
19. Jossen V, Muoio F, Panella S, Harder Y, Tallone T, Eibl R (2020) An approach towards a GMP compliant in-vitro expansion of human adipose stem cells for autologous therapies. *Bioengineering* 7(3):77–100
20. Reichardt A, Polchow B, Shakibaei M, Henrich W, Hetzer R, Lueders C (2013) Large scale expansion of human umbilical cord cells in a rotating bed system bioreactor for cardiovascular tissue engineering applications. *Open Biomed Eng J* 7:50–61. <https://doi.org/10.2174/1874120701307010050>
21. Ikebe C, Suzuki K (2014) Mesenchymal stem cells for regenerative therapy: optimization of cell preparation protocols. *Biomed Res Int* 2014:1–11. <https://doi.org/10.1155/2014/951512>
22. Scibona E, Morbidelli M (2019) Expansion processes for cell-based therapies. *Biotechnol Adv* 37:107455. <https://doi.org/10.1016/j.biotechadv.2019.107455>
23. Discher DE, Mooney DJ, Zandstra PW (2010) Growth factors, matrices, and forces combine. *Growth (Lakeland)* 324:1673–1677. <https://doi.org/10.1126/science.1171643.Growth>
24. Steward AJ, Kelly DJ (2015) Mechanical regulation of mesenchymal stem cell differentiation. *J Anat* 227:717–731. <https://doi.org/10.1111/joa.12243>
25. Kaiser SC, Eibl D, Eibl R (2015) Single-use bioreactors for animal and human cells. In: *Animal cell culture: cell engineering*. Springer, Cham, pp 445–499
26. Baraniak PR, McDevitt TC (2012) Scaffold-free culture of mesenchymal stem cell spheroids in suspension preserves multilineage potential. *Cell Tissue Res* 347:701–711. <https://doi.org/10.1007/s00441-011-1215-5>
27. Frith JE, Thomson B, Genever PG (2010) Dynamic three-dimensional culture methods enhance mesenchymal stem cell properties and increase therapeutic potential. *Tissue Eng Part C Methods* 16:735–749. <https://doi.org/10.1089/ten.tec.2009.0432>
28. Alimperti S, Lei P, Wen Y, Tian J, Campbell AM, Andreadis ST (2014) Serum-free spheroid suspension culture maintains mesenchymal stem cell proliferation and differentiation potential. *Biotechnol Prog* 30:974–983. <https://doi.org/10.1002/btpr.1904>
29. Allen LM, Matyas J, Ungrin M, Hart DA, Sen A (2019) Serum-free culture of human mesenchymal stem cell aggregates in suspension bioreactors for tissue engineering applications. *Stem Cells Int* 2019:1–18. <https://doi.org/10.1155/2019/4607461>
30. Bhang SH, Cho S-W, La W-G, Lee T-J, Yang HS, Sun A-Y, Baek S-H, Rhie J-W, Kim B-S (2011) Angiogenesis in ischemic tissue produced by spheroid grafting of human adipose-derived stromal cells. *Biomaterials* 32:2734–2747. <https://doi.org/10.1016/j.biomaterials.2010.12.035>
31. Layer PG, Robitzki A, Rothermel A, Willbold E (2002) Of layers and spheres: the reaggregate approach in tissue engineering. *Trends Neurosci* 25:131–134. [https://doi.org/10.1016/S0166-2236\(00\)02036-1](https://doi.org/10.1016/S0166-2236(00)02036-1)
32. Achilli T-M, Meyer J, Morgan JR (2012) Advances in the formation, use and understanding of multi-cellular spheroids. *Expert Opin Biol Ther* 12:1347–1360. <https://doi.org/10.1517/14712598.2012.707181>
33. Page H, Flood P, Reynaud EG (2013) Three-dimensional tissue cultures: current trends and beyond. *Cell Tissue Res* 352:123–131. <https://doi.org/10.1007/s00441-012-1441-5>
34. Edmondson R, Broglie JJ, Adcock AF, Yang L (2014) Three-dimensional cell culture systems and their applications in drug discovery and cell-based biosensors. *Assay Drug Dev Technol* 12:207–218. <https://doi.org/10.1089/adt.2014.573>
35. Caron MMJ, Emans PJ, Coolsen MME, Voss L, Surtel DAM, Cremers A, van Rhijn LW, Welting TJM (2012) Redifferentiation of dedifferentiated human articular chondrocytes: comparison of 2D and 3D cultures. *Osteoarthr Cartil* 20:1170–1178. <https://doi.org/10.1016/j.joca.2012.06.016>
36. Bourin P, Bunnell BA, Casteilla L, Dominici M, Katz AJ, March KL, Redl H, Rubin JP, Yoshimura K, Gimble JM (2013) Stromal cells from the adipose tissue-derived stromal

- vascular fraction and culture expanded adipose tissue-derived stromal/stem cells: a joint statement of the International Federation for Adipose Therapeutics and Science (IFATS) and the International So. Cytotherapy 15:641–648. <https://doi.org/10.1016/j.jcyt.2013.02.006>
37. Dominici M, Le Blanc K, Mueller I, Slaper-Cortenbach I, Marini F, Krause D, Deans R, Keating A, Prockop D, Horwitz E (2006) Minimal criteria for defining multipotent mesenchymal stromal cells. The International Society for Cellular Therapy position statement. *Cytotherapy* 8:315–317. <https://doi.org/10.1080/14653240600855905>
 38. Cheng N-C, Chen S-Y, Li J-R, Young T-H (2013) Short-term spheroid formation enhances the regenerative capacity of adipose-derived stem cells by promoting stemness, angiogenesis, and chemotaxis. *Stem Cells Transl Med* 2:584–594. <https://doi.org/10.5966/sctm.2013-0007>
 39. Bartosh TJ, Ylostalo JH, Mohammadipour A, Bazhanov N, Coble K, Claypool K, Lee RH, Choi H, Prockop DJ (2010) Aggregation of human mesenchymal stromal cells (MSCs) into 3D spheroids enhances their antiinflammatory properties. *Proc Natl Acad Sci* 107:13724–13729. <https://doi.org/10.1073/pnas.1008117107>
 40. YlÖstalo JH, Bartosh TJ, Coble K, Prockop DJ (2012) Human mesenchymal stem/stromal cells cultured as spheroids are self-activated to produce prostaglandin E2 that directs stimulated macrophages into an anti-inflammatory phenotype. *Stem Cells* 30:2283–2296. <https://doi.org/10.1002/stem.1191>
 41. Zimmermann JA, Mcdevitt TC (2014) Pre-conditioning mesenchymal stromal cell spheroids for immunomodulatory paracrine factor secretion. *Cytotherapy* 16:331–345. <https://doi.org/10.1016/j.jcyt.2013.09.004>
 42. Horn P, Bokermann G, Cholewa D, Bork S, Walenda T, Koch C, Drescher W, Hutschenreuther G, Zenke M, Ho AD, Wagner W (2010) Impact of individual platelet lysates on isolation and growth of human mesenchymal stromal cells. *Cytotherapy* 12:888–898. <https://doi.org/10.3109/14653249.2010.501788>
 43. Badenes SM, Fernandes TG, Rodrigues CAV, Diogo MM, Cabral JMS (2016) Microcarrier-based platforms for in vitro expansion and differentiation of human pluripotent stem cells in bioreactor culture systems. *J Biotechnol* 234:71–82. <https://doi.org/10.1016/j.jbiotec.2016.07.023>
 44. Villa-Diaz LG, Ross AM, Lahann J, Krebsbach PH (2013) Concise review: the evolution of human pluripotent stem cell culture: from feeder cells to synthetic coatings. *Stem Cells* 31:1–7. <https://doi.org/10.1002/stem.1290>
 45. Shearier E, Xing Q, Qian Z, Zhao F (2016) Physiologically low oxygen enhances biomolecule production and stemness of mesenchymal stem cell spheroids. *Tissue Eng Part C Methods* 22:360–369. <https://doi.org/10.1089/ten.tec.2015.0465>
 46. Wu J, Rostami MR, Cadavid Olaya DP, Tzanakakis ES (2014) Oxygen transport and stem cell aggregation in stirred-suspension bioreactor cultures. *PLoS One* 9:e102486. <https://doi.org/10.1371/journal.pone.0102486>
 47. Lei Y, Schaffer DV (2013) A fully defined and scalable 3D culture system for human pluripotent stem cell expansion and differentiation. *Proc Natl Acad Sci* 110:E5039–E5048. <https://doi.org/10.1073/pnas.1309408110>
 48. Sart S, Tsai A-C, Li Y, Ma T (2014) Three-dimensional aggregates of mesenchymal stem cells: cellular mechanisms, biological properties, and applications. *Tissue Eng Part B Rev* 20:365–380. <https://doi.org/10.1089/ten.teb.2013.0537>
 49. Sucusky P, Osorio DF, Brown JB, Neitzel GP (2004) Fluid mechanics of a spinner-flask bioreactor. *Biotechnol Bioeng* 85:34–46. <https://doi.org/10.1002/bit.10788>
 50. Kaiser S, Jossen V, Schirmaier C, Eibl D, Brill S, van den Bos C, Eibl R (2013) Fluid flow and cell proliferation of mesenchymal adipose-derived stem cells in small-scale, stirred, single-use bioreactors. *Chem Ing Tech* 85:95–102. <https://doi.org/10.1002/cite.201200180>
 51. von Weizel AL (1967) Growth of cell-strains and primary cells on microcarriers in homogeneous culture. *Nature* 216:64–65

52. Chen AK-L, Reuveny S, Oh SKW (2013) Application of human mesenchymal and pluripotent stem cell microcarrier cultures in cellular therapy: achievements and future direction. *Biotechnol Adv* 31:1032–1046. <https://doi.org/10.1016/j.biotechadv.2013.03.006>
53. Jossen V, van den Bos C, Eibl R, Eibl D (2018) Manufacturing human mesenchymal stem cells at clinical scale: process and regulatory challenges. *Appl Microbiol Biotechnol* 102:3981–3994. <https://doi.org/10.1007/s00253-018-8912-x>
54. Rafiq QA, Ruck S, Hanga MP, Heathman TRJ, Coopman K, Nienow AW, Williams DJ, Hewitt CJ (2018) Qualitative and quantitative demonstration of bead-to-bead transfer with bone marrow-derived human mesenchymal stem cells on microcarriers: utilising the phenomenon to improve culture performance. *Biochem Eng J* 135:11–21. <https://doi.org/10.1016/j.bej.2017.11.005>
55. Leber J, Barezkai J, Blumenstock M, Pospisil B, Salzig D, Czermak P (2017) Microcarrier choice and bead-to-bead transfer for human mesenchymal stem cells in serum-containing and chemically defined media. *Process Biochem* 59:255–265. <https://doi.org/10.1016/j.procbio.2017.03.017>
56. Szczypka M, Splan D, Woolls H, Brandwein H (2014) Single-use bioreactors and microcarriers. *Bioprocess Int* 12:54–64
57. Zhao L-G, Chen S-L, Teng Y-J, An L-P, Wang J, Ma J-L, Xia Y-Y (2014) The MEK5/ERK5 pathway mediates fluid shear stress promoted osteoblast differentiation. *Connect Tissue Res* 55:96–102. <https://doi.org/10.3109/03008207.2013.853755>
58. Yim EK, Sheetz MP (2012) Force-dependent cell signaling in stem cell differentiation. *Stem Cell Res Ther* 3:41. <https://doi.org/10.1186/scrt132>
59. Frauenschuh S, Reichmann E, Ibold Y, Goetz PM, Sittlinger M, Ringe J (2007) A microcarrier-based cultivation system for expansion of primary mesenchymal stem cells. *Biotechnol Prog* 23:187–193. <https://doi.org/10.1021/bp060155w>
60. Panchalingam KM, Jung S, Rosenberg L, Behie LA (2015) Bioprocessing strategies for the large-scale production of human mesenchymal stem cells: a review. *Stem Cell Res Ther* 6:225. <https://doi.org/10.1186/s13287-015-0228-5>
61. Ferrari C, Balandras F, Guedon E, Olmos E, Chevalot I, Marc A (2012) Limiting cell aggregation during mesenchymal stem cell expansion on microcarriers. *Biotechnol Prog* 28:780–787. <https://doi.org/10.1002/btpr.1527>
62. Schirmaier C, Jossen V, Kaiser SC, Jüngerkes F, Brill S, Safavi-Nab A, Siehoff A, van den Bos C, Eibl D, Eibl R (2014) Scale-up of adipose tissue-derived mesenchymal stem cell production in stirred single-use bioreactors under low-serum conditions. *Eng Life Sci* 14:292–303. <https://doi.org/10.1002/elsc.201300134>
63. Lawson T, Kehoe DE, Schnitzler AC, Rapijko PJ, Der KA, Philbrick K, Punreddy S, Rigby S, Smith R, Feng Q, Murrell JR, Rook MS (2017) Process development for expansion of human mesenchymal stromal cells in a 50L single-use stirred tank bioreactor. *Biochem Eng J* 120:49–62. <https://doi.org/10.1016/j.bej.2016.11.020>
64. Gruber R, Karreth F, Kandler B, Fuerst G, Rot A, Fischer AB (2004) Platelet-released supernatants increase migration and proliferation, and decrease osteogenic differentiation of bone marrow-derived mesenchymal progenitor cell under in vitro conditions. *Platelets* 15:29–35
65. Lange C, Cakiroglu F, Spiess AN, Cappallo-Obermann H, Dierlamm J, Zander AR (2007) Accelerated and safe expansion of human mesenchymal stromal cells in animal serum-free medium for transplantation and regenerative medicine. *J Cell Physiol* 213:18–26
66. Abdelrazik H, Spaggiari GM, Chiassone L, Mretta L (2011) Mesenchymal stem cells expanded in human platelet lysate display a decreased inhibitory capacity on T- and NK-cell proliferation and function. *Eur J Immunol* 41:3281–3290
67. Heathman TRJJ, Glyn VAM, Picken A, Rafiq QA, Coopman K, Nienow AW, Kara B, Hewitt CJ (2015) Expansion, harvest and cryopreservation of human mesenchymal stem cells in a serum-free microcarrier process. *Biotechnol Bioeng* 112:1696–1707. <https://doi.org/10.1002/bit.25582>

68. Carmelo JG, Fernandes-Platzgummer A, Diogo MM, da Silva CL, Cabral JMS (2015) A xeno-free microcarrier-based stirred culture system for the scalable expansion of human mesenchymal stem/stromal cells isolated from bone marrow and adipose tissue. *Biotechnol J* 10:1235–1247. <https://doi.org/10.1002/biot.201400586>
69. Rafiq QA, Coopman K, Nienow AW, Hewitt CJ (2016) Systematic microcarrier screening and agitated culture conditions improves human mesenchymal stem cell yield in bioreactors. *Biotechnol J* 11:473–486. <https://doi.org/10.1002/biot.201400862>
70. Heathman TRJ, Stolzing A, Fabian C, Rafiq QA, Coopman K, Nienow AW, Kara B, Hewitt CJ (2016) Scalability and process transfer of mesenchymal stromal cell production from monolayer to microcarrier culture using human platelet lysate. *Cytotherapy* 18:523–535. <https://doi.org/10.1016/j.jcyt.2016.01.007>
71. Nienow AW, Hewitt CJ, Heathman TRJ, Glyn VAM, Fonte GN, Hanga MP, Coopman K, Rafiq QA (2016) Agitation conditions for the culture and detachment of hMSCs from microcarriers in multiple bioreactor platforms. *Biochem Eng J* 108:24–29. <https://doi.org/10.1016/j.bej.2015.08.003>
72. Dufey V, Tachenay A, Art M, Becken U, De Longueville F (2016) Expansion of human bone marrow-derived mesenchymal stem cells in BioBLU 0.3c single-use bioreactors. *Appl Note* 305:1–8
73. Heathman TRJ, Nienow AW, Rafiq QA, Coopman K, Bo K, Hewitt CJ (2019) Development of a process control strategy for the serum-free microcarrier expansion of human mesenchymal stem cells towards cost-effective and commercially viable manufacturing. *Biochem Eng J* 141:200–209. <https://doi.org/10.1016/j.bej.2018.10.018>
74. Jossen V, Kaiser SC, Schirmaier C, Herrmann J, Tappe A, Eibl D, Siehoff A, van d BC, Eibl R (2014) Modification and qualification of a stirred single-use bioreactor for the improved expansion of human mesenchymal stem cells at benchtop scale. *Pharm Bioprocess* 2:311–322. <https://doi.org/10.4155/pbp.14.29>
75. Jossen V, Pörtner R, Kaiser SC, Kraume M, Eibl D, Eibl R (2014) Mass production of mesenchymal stem cells – impact of bioreactor design and flow conditions on proliferation and differentiation. In: Eberli D (ed) *Cells and biomaterials in regenerative medicine*. InTech, Rijeka, pp 119–174
76. Siddiquee K, Sha M (2014) Large-scale production of human mesenchymal stem cells in BioBLU 5c single-use vessels
77. Bery JD, Liovic P, Šutalo ID, Stewart RL, Glattauer V, Meagher L (2016) Characterisation of stresses on microcarriers in a stirred bioreactor. *App Math Model* 40:6787–6804. <https://doi.org/10.1016/j.apm.2016.02.025>
78. Paschedag AR (2004) *CFD in der Vevfahrenstechnik*. Wiley-VCH Verlag GmbH & Co.
79. Ferziger JH, Peric M, Leonard A (1997) Computational methods for fluid dynamics. *Phys Today* 50:80–84. <https://doi.org/10.1063/1.881751>
80. Rodriguez S (2019) *Applied computational fluid dynamics and turbulence modeling*. Springer International Publishing, Cham
81. Delafosse A, Collignon M-L, Marc A, Toye D, Olmos E (2015) Revisiting the determination of hydromechanical stresses encountered by microcarriers in stem cell culture bioreactors. *BMC Proc* 9:P41. <https://doi.org/10.1186/1753-6561-9-S9-P41>
82. Liovic P, Šutalo ID, Stewart R, Glattauer V, Meagher L (2012) Fluid flow and stresses on microcarriers in spinner flask bioreactors. *Ninth Int Conf CFD Miner Process Ind*:1–6
83. Delafosse A, Calvo S, Collignon M-L, Delvigne F, Crine M, Toye D (2015) Euler–Lagrange approach to model heterogeneities in stirred tank bioreactors – comparison to experimental flow characterization and particle tracking. *Chem Eng Sci* 134:457–466. <https://doi.org/10.1016/j.ces.2015.05.045>
84. Nienow AW, Rielly CD, Brosnan K, Bargh N, Lee K, Coopman K, Hewitt CJ (2013) The physical characterisation of a microscale parallel bioreactor platform with an industrial CHO cell line expressing an IgG4. *Biochem Eng J* 76:25–36. <https://doi.org/10.1016/j.bej.2013.04.011>

85. Collignon M-L, Delafosse A, Calvo S, Martin C, Marc A, Toye D, Olmos E (2016) Large-Eddy simulations of microcarrier exposure to potentially damaging eddies inside mini-bioreactors. *Biochem Eng J* 108:30–43. <https://doi.org/10.1016/j.bej.2015.10.020>
86. Kunas KT, Papoutsakis ET (1990) The protective effect of serum against hydrodynamic damage of hybridoma cells in agitated and surface-aerated bioreactors. *J Biotechnol* 15:57–69. [https://doi.org/10.1016/0168-1656\(90\)90051-C](https://doi.org/10.1016/0168-1656(90)90051-C)
87. Michaels JD, Petersen JF, McIntire LV, Papoutsakis ET (1991) Protection mechanisms of freely suspended animal cells (CRL 8018) from fluid-mechanical injury. Viscometric and bioreactor studies using serum, pluronic F68 and polyethylene glycol. *Biotechnol Bioeng* 38:169–180. <https://doi.org/10.1002/bit.260380209>
88. Chisti Y (2000) Animal-cell damage in sparged bioreactors. *Trends Biotechnol* 18:420–432. [https://doi.org/10.1016/S0167-7799\(00\)01474-8](https://doi.org/10.1016/S0167-7799(00)01474-8)
89. Jossen V (2020) Bioengineering aspects of microcarrier-based hMSC expansions in different single-use bioreactors. Technical University of Berlin, Berlin
90. Stoots CM, Calabrese RV (1995) Mean velocity field to a rushton turbine blade. *Am Inst Chem Eng J* 41:1–11
91. Wollny S (2010) Experimentelle und numerische Untersuchungen zur Partikelbeanspruchung in gerührten (Bio-)Reaktoren. Technical University of Berlin
92. Venkat RV, Stock LR, Chalmers JJ (2000) Study of hydrodynamics in microcarrier culture spinner vessels: a particle tracking velocimetry approach. *Biotechnol Bioeng* 49:456–466. [https://doi.org/10.1002/\(SICI\)1097-0290\(19960220\)49:4<456::AID-BIT13>3.0.CO;2-8](https://doi.org/10.1002/(SICI)1097-0290(19960220)49:4<456::AID-BIT13>3.0.CO;2-8)
93. Ismadi M-Z, Hourigan K, Fouras A (2014) Experimental characterisation of fluid mechanics in a spinner flask bioreactor. *Processes* 2:753–772. <https://doi.org/10.3390/pr2040753>
94. Zhang H, Lamping SR, Pickering SCR, Lye GJ, Shamlou PA (2008) Engineering characteristics of a single well from 24-well and 96-well microtitre plates. *Biochem Eng J* 40:138–149
95. Godara P, McFarland CD, Nordon RE (2008) Design of bioreactors for mesenchymal stem cell tissue engineering. *J Chem Technol Biotechnol* 83:408–420. <https://doi.org/10.1002/jctb.1918>
96. Rafiq QA, Brosnan KM, Coopman K, Nienow AW, Hewitt CJ (2013) Culture of human mesenchymal stem cells on microcarriers in a 5 l stirred-tank bioreactor. *Biotechnol Lett* 35:1233–1245. <https://doi.org/10.1007/s10529-013-1211-9>
97. Ibrahim S, Nienow AW (2004) Suspension of microcarriers for cell culture with axial flow impellers. *Chem Eng Res Des* 82:1082–1088. <https://doi.org/10.1205/cerd.82.9.1082.44161>
98. Hewitt CJ, Lee K, Nienow AW, Thomas RJ, Smith M, Thomas CR (2011) Expansion of human mesenchymal stem cells on microcarriers. *Biotechnol Lett* 33:2325–2335. <https://doi.org/10.1007/s10529-011-0695-4>
99. Yourek G, McCormick SM, Mao JJ, Reilly GC (2010) Shear stress induces osteogenic differentiation of human mesenchymal stem cells. *Regen Med* 5:713–724. <https://doi.org/10.2217/rme.10.60>
100. Yourek G, Hussain MA, Mao JJ (2007) Cytoskeletal changes of mesenchymal stem cells during differentiation. *ASAIO J* 53:219–228. <https://doi.org/10.1097/MAT.0b013e31802deb2d>
101. Yeatts AB, Choquette DT, Fisher JP (2013) Bioreactors to influence stem cell fate: augmentation of mesenchymal stem cell signaling pathways via dynamic culture systems. *Biochim Biophys Acta Gen Subj* 1830:2470–2480. <https://doi.org/10.1016/j.bbagen.2012.06.007>
102. Yeatts AB, Fisher JP (2011) Bone tissue engineering bioreactors: dynamic culture and the influence of shear stress. *Bone* 48:171–181. <https://doi.org/10.1016/j.bone.2010.09.138>
103. Weyand B, Reimers K, Vogt PM (2011) Influences of extracellular matrix properties and flow shear stresses on stem cell shape in a three-dimensional dynamic environment. *IFMBE Proc* 30:47–50
104. Weyand B, Kasper C, Israelowitz M, Gille C, von Schroeder HP, Reimers K, Vogt PM (2012) A differential pressure laminar flow reactor supports osteogenic differentiation and

- extracellular matrix formation from adipose mesenchymal stem cells in a macroporous ceramic scaffold. *Biores Open Access* 1:145–157
105. Weyand B, Israelowitz M, von Schroeder HP, Vogt PM (2009) Fluid dynamics in bioreactor design: considerations for the theoretical and practical approach. *Adv Biochem Eng Biotechnol* 112:251–268
 106. Croughan MS, Hamel J-F, Wang DIC (2006) Hydrodynamic effects on animal cells grown in microcarrier cultures. *Biotechnol Bioeng* 95:295–305. <https://doi.org/10.1002/bit.21158>
 107. Heathman TRJ, Stolzing A, Fabian C, Rafiq QA, Coopman K, Nienow AW, Kara B, Hewitt CJ (2015) Serum-free process development: improving the yield and consistency of human mesenchymal stromal cell production. *Cytotherapy* 17:1524–1535. <https://doi.org/10.1016/j.jcyt.2015.08.002>
 108. Cierpka K, Elseberg CL, Niss K, Kassem M, Salzig D, Czermak P (2013) hMSC production in disposable bioreactors with regards to GMP and PAT. *Chem Ing Tech* 85:67–75. <https://doi.org/10.1002/cite.201200151>
 109. Rafiq QA, Hanga MP, Heathman TRJ, Coopman K, Nienow AW, Williams DJ, Hewitt CJ (2017) Process development of human multipotent stromal cell microcarrier culture using an automated high-throughput microbioreactor. *Biotechnol Bioeng* 114:2253–2266. <https://doi.org/10.1002/bit.26359>
 110. Higuera G, Schop D, Janssen F, van Dijkhuizen-Radersma R, van Boxtel T, van Blitterswijk CA (2009) Quantifying in vitro growth and metabolism kinetics of human mesenchymal stem cells using a mathematical model. *Tissue Eng Part A* 15:2653–2663. <https://doi.org/10.1089/ten.tea.2008.0328>
 111. dos Santos F, Andrade PZ, Boura JS, Abecasis MM, da Silva CL, Cabral JMS (2009) Ex vivo expansion of human mesenchymal stem cells: a more effective cell proliferation kinetics and metabolism under hypoxia. *J Cell Physiol* 223:n/a–n/a. <https://doi.org/10.1002/jcp.21987>
 112. Bartolini E, Manoli H, Costamagna E, Jeyaseelan HA, Hamad M, Irhimeh MR, Khademhosseini A, Abbas A (2015) Population balance modelling of stem cell culture in 3D suspension bioreactors. *Chem Eng Res Des* 101:125–134. <https://doi.org/10.1016/j.cherd.2015.07.014>
 113. Mancuso L, Ilaria Liuzzo M, Fadda S, Cincotti A, Pisu M, Concas A, Cao G (2010) Experimental analysis and modeling of bone marrow mesenchymal stem cells proliferation. *Chem Eng Sci* 65:562–568. <https://doi.org/10.1016/j.ces.2009.06.034>
 114. Bailón-Plaza A, van der Meulen MCH (2001) A mathematical framework to study the effects of growth factor influences on fracture healing. *J Theor Biol* 212:191–209. <https://doi.org/10.1006/jtbi.2001.2372>
 115. Geris L, Peiffer V, Demol J, Oosterwyck H Van (2006) Modelling of in vitro mesenchymal stem cell cultivation, chondrogenesis and osteogenesis. *J Biomech* 41:466–466
 116. Schellenberg A, Stiehl T, Horn P, Joussem S, Pallua N, Ho AD, Wagner W (2012) Population dynamics of mesenchymal stromal cells during culture expansion. *Cytotherapy* 14:401–411. <https://doi.org/10.3109/14653249.2011.640669>
 117. Cholewa D, Stiehl T, Schellenberg A, Bokermann G, Joussem S, Koch C, Walenda T, Pallua N, Marciniak-Czochra A, Suschek CV, Wagner W (2011) Expansion of adipose mesenchymal stromal cells is affected by human platelet lysate and plating density. *Cell Transplant* 20:1409–1422. <https://doi.org/10.3727/096368910X557218>
 118. Hoffmann M, Kuska J-P, Zscharnack M, Loeffler M, Galle J (2011) Spatial organization of mesenchymal stem cells in vitro – results from a new individual cell-based model with podia. *PLoS One* 6:e21960. <https://doi.org/10.1371/journal.pone.0021960>